Active and Passive Components for Broadband Transmit Phased Arrays

Laila Marzall, Megan Robinson, Paige Danielson, Amy Robinson, Negar Ehsan, and Zoya Popović

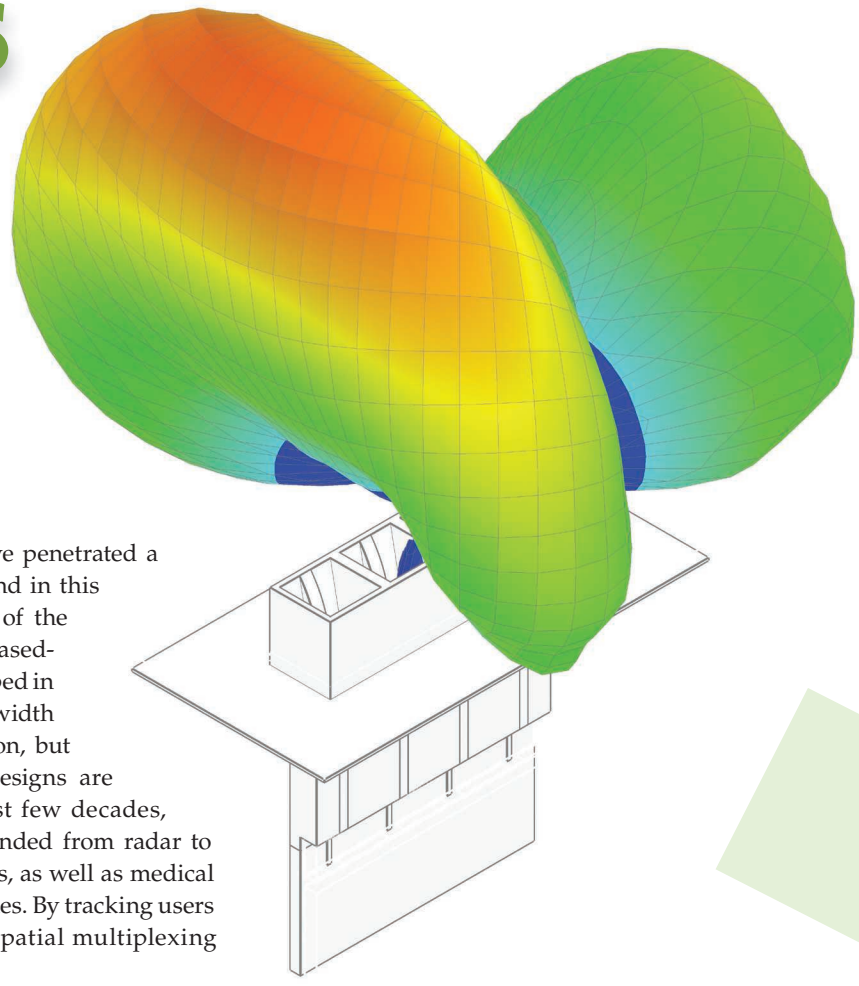

Phased-array antennas have penetrated a large application space, and in this article, we present some of the critical components for phased-array front ends, as described in Figure 1. We focus on an octave-bandwidth 6- to 12-GHz transmit implementation, but the methodology and component designs are scalable in frequency. Over the past few decades, phased-array applications have expanded from radar to wireless and satellite communications, as well as medical imaging and various sensing modalities. By tracking users with individual high-gain beams, spatial multiplexing

Laila Marzall (laila.marzall@colorado.edu), Megan Robinson (megan.robinson@colorado.edu), Paige Danielson (paige.danielson@colorado.edu), and Amy Robinson (amy.robinson@colorado.edu) are with the University of Colorado, Boulder, Colorado, 80309, USA. Negar Ehsan (negar.ehsan@nasa.gov) is with NASA Goddard Space Flight Center, Greenbelt, Maryland, 20771, USA. Zoya Popović (zoya.popovic@colorado.edu) is with the University of Colorado, Boulder, Colorado, 80309, USA.

Digital Object Identifier 10.1109/MMM.2021.3125465

Date of current version: 11 January 2022

enables cochannel interference mitigation, enhancing signal levels, and power management in wireless communications systems. For example, [1] shows a 64-element phased-array transceiver operating in the 28-GHz band with 52-dBm effective isotropic radiated power (EIRP) for 5G applications with up to 12 Gb/s of throughput, and [2] demonstrates a system-level development of a 384-element, 16-tile, W-band phased array with 52-dBm EIRP in 0.18-μm silicon–germanium bipolar CMOS (BiCMOS) technology. In satellite broadcasting and communication systems, phased-array antennas enable beam shaping over countries and continents, tracking at the end-user side, and rain fading mitigation, e.g., [3]. In [4], advances in phased arrays for satellite applications developed at Lockheed Martin are described from an industry perspective.

Phased arrays also provide enhanced capabilities for airborne radar: power efficiency increase; adaptive beamforming to suppress jammers; space-time adaptive processing to suppress clutter return; multibeam on receive capability for multistatic operation in stealth target detection; and higher system availability due to graceful degradation of array performance resulting in low lifecycle cost [5]. For fast mobile applications, automotive radars are used as sensors for adaptive cruise-control (ACC), safety applications like blind-spot surveillance and collision mitigation/avoidance, backing/parking, and low-speed/stop-and-go ACC [6]. In [7], a system simulation using a phased-array frequency-modulated continuous-wave radar with beam steering controlled by environmental variables is implemented, demonstrating the advantages of increased range and providing more time for adaptation. The automotive environment presents design challenges such as packaging and a harsh thermomechanical environment. In [6], automotive radar front-end phased array are analyzed, where RF microelectromechanical systems (MEMS) are used as switches in a Rotman lens or in phase shifters and optimized for RF and thermomechanical behavior.

For weather monitoring, phased-array radars bring the capability of scanning bigger volumes in shorter time intervals achieving update rates of < 1 mm [8], where beam control and null generation enable collecting robust data for post-statistical analysis [9]. Also, phased arrays have found applications in RFID for localization in the ultrahigh frequency range, e.g., [10], while in radio astronomy [11], adaptive nulling techniques help combat radio frequency interference [12]. More recently, beam-steering techniques have been extended to biomedical devices [13]. Doppler-based noncontact vital-sign (NCVS) sensor systems are used to monitor heart and respiration rates of patients. The sensor accuracy can deteriorate quickly in a noisy or cluttered environment, and [14] reports on directive phased arrays for NCVS systems with considerably improved accuracy compared to fixed-beam Doppler radar. In [15], a 70-MHz near-field phased array provides 3D specific absorption rate control and increases locoregional hyperthermia in tumor treatments, while in magnetic resonance imaging systems signal-to-noise ratio, image contrast and resolution can be improved [16]. Phased arrays are also applied in wireless power transfer systems for maximizing power delivery to an intended location while minimizing leakage fields in other locations, e.g., [17].

The growing variety of applications and system requirements lead to the need of scalable, modularized devices for transmit and receive chains. In this context, [18], e.g., shows heterogeneously-integrated phased arrays for communication and sensor applications at Ku-band. In the transmit chain, spatial power combining is used to increase the EIRP, where each element or subarray is fed by an independent RF front-end circuit. This approach allows operation with multiple signals and beams using the same fixed antenna aperture, with tradeoffs in size and performance requirements for high-power, wideband operation [19]. Although it is an effective method to increase radiated power, size and generated heat remain key limitation as frequency increases and the $\lambda_0/2$ spacing of the antennas shrinks slower than the size of active elements. Therefore, power density and efficiency of the power amplifiers (PAs) favor the use of gallium nitride (GaN) over gallium arsenide (GaAs). The high breakdown voltage of GaN results in high peak power levels and is accompanied by a robust silicon carbide (SiC) substrate with good thermal conductivity. Trends in active arrays for space and radar applications, with GaAs replaced by GaN PAs to increase EIRP with the same number of elements are discussed in [20] and [21].

Instantaneous bandwidth and complex modulation schemes place broadband operation demands on microwave circuits. Although most phased arrays are relatively narrowband, a number of arrays with broadband optical beamforming, e.g., [22], and CMOS true-time delay beamformers, e.g., [23], have been demonstrated. A comprehensive overview of digital and hybrid approaches can be found in, e.g., [24]–[26].

This article addresses microwave and millimeter-wave active and passive components for broadband-phased array front ends, focusing mostly on the transmit path. Figure 1 shows a high-level block diagram that outlines the article content. The main blocks include the beamforming network, amplification stage, isolation stage between transmit and receive, and the final radiating aperture. The digital control and dc supply are not discussed here but are an integral part of the system. The last component in the chain is the passive antenna itself, and its radiating and matching

The growing variety of applications and system requirements lead to the need of scalable, modularized devices for transmit and receive chains.

characteristics affect the entire system performance. More specifically, the coupling between antenna elements results in an active scan impedance that varies across the array and across frequency and scan angle, as overviewed in, e.g., [27].

We present previous and ongoing studies of the transmit-chain front-end components shown in Figure 1, including design approaches and performance tradeoff analyses. The "Beamforming Networks" section overviews three broadband analog beamforming approaches: octave-bandwidth monolithic microwave integrated circuit (MMIC) phase shifters based on loaded transmission lines; an octave-bandwidth Butler matrix; and a millimeter-wave frequency-steered array. The "Isolation Circuits" section presents a 7–13-GHz MMIC active circulator and a broadband analog method for canceling self-interference in the receive path. In the "Analysis of PAs in a Phased-Array Environment" section, a broadband nonlinear analysis for the transmit chain is shown, including the effects of antenna element mismatch due to scanning. The "Discussion and Outlook" section introduces a quantum sensor with a potential for broadband traceable electric field measurements as a method for near-field array calibration and a supply modulation as an efficiency enhancement technique for PAs on the example of a three-stage 18–25-GHz MMIC PA. Throughout the article, we focus on III–V semiconductor (GaAs and GaN) MMICs for the active components with potential for heterogeneous integration.

Beamforming Networks

In the case of broadband-phased arrays, beam squint can be mitigated using true-time delay beamforming, which can be done in the optical or microwave domains. Common microwave true-time delay phase

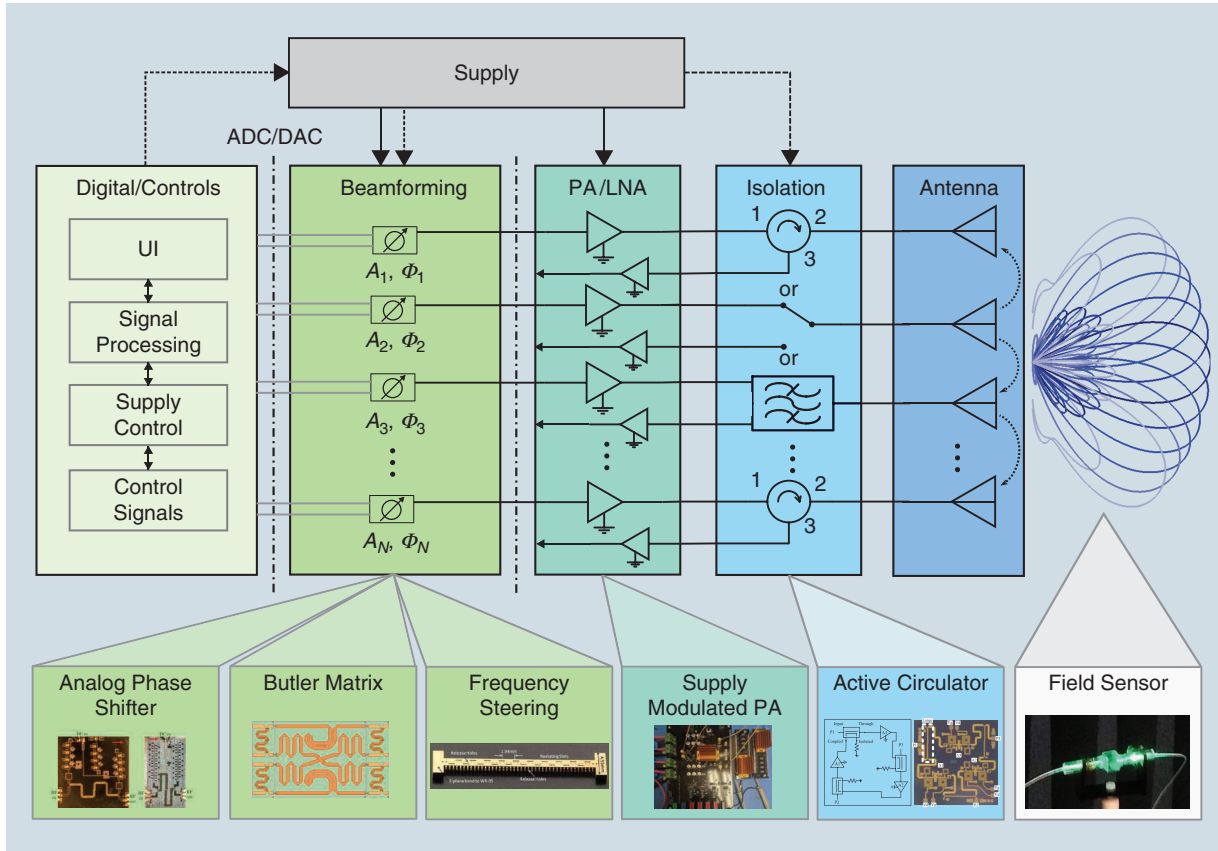

Figure 1. *A high-level block diagram of a phased array, where the beamforming can be done either in the digital or analog domains. The dotted arrows indicate coupling between the antenna elements. The focus of this article is on analog components of broadband transmit arrays, including beamforming networks, amplification, isolation, and field measurements. Shown in the expanded blocks with photographs are MMIC phase shifters, a Butler matrix, and frequency scanning as the beamformer networks; MMIC PAs; MMIC active circulators; and field sensors for aperture electrometry. Past and ongoing research at the University of Colorado, related to the design of these components, is described throughout the article.*

shifters include loaded lines [28] and switched delay lines [29]. In the next section,"Broadband GaAs and GaN MMIC Phase Shifters for Beamforming," continuous analog phase shifters and a corporate feed network in the 6–12 GHz octave band are discussed. Discrete beams can be achieved with other true-time delay feed networks, such as Butler and Blass matrices, and Rotman and Luneburg lenses [27]. Later in this section, a Butler matrix covering the 6–12-GHz octave band is presented. These approaches do not scale favorably to higher millimeter-wave frequencies, where phase shifters and transmission-line elements are too lossy. Therefore, an approach that can use a lower-frequency VCO and frequency multiplier as the input is studied on the example of a 130–180-GHz microfabricated broadband sequentially fed frequency-steered array for planetary-landing radar, described in the last part of this section.

Broadband GaAs and GaN MMIC Phase Shifters for Beamforming

Loaded transmission lines can provide a true-time delay over as much as a decade bandwidth, where the phase is varied using varactors [29], MEMS [28] or ferroelectrics [30] and are typically limited by return loss variation over frequency. Reflective phase shifters with different hybrids are presented in [31], [32], and the variable reflective loads can be implemented with MEMS or varactors. Large continuous phase shifts in [33], [34], are accomplished with two cascaded phase shifters. To achieve a good match and large phase shift across an octave band (6–12 GHz), we demonstrate the circuit in Figure 2, which combines a reflective topology with a loaded-line variable reactance. To showcase the architecture and investigate nonlinear performance, a GaAs MMIC with a phase that increases over the band, and a GaN MMIC with maximum phase shift in the center of the band are designed [35].

The phase shifter MMICs are implemented in WIN Semiconductors' GaAs enhancement (E-) mode PIH10 and GaN depletion (D-) mode NP15-00 pseudomorphic high electron-mobility transistor (pHEMPT) processes. The periphery of the transistors is chosen to approximately scale with power density of the processes: $4 \times 75\ \mu$m in GaAs (≈ 1.5 W/mm) and $2 \times 75\ \mu$m in GaN (≈ 3.5 W/mm). Each variable capacitor in Figure 2 is implemented with a transistor with grounded source and drain terminals. For the GaAs E-mode devices, the capacitance varies with gate bias (–0.2 to 0.6 V) from 0.241 to 0.470 pF at 9 GHz. The GaAs phase shifter uses

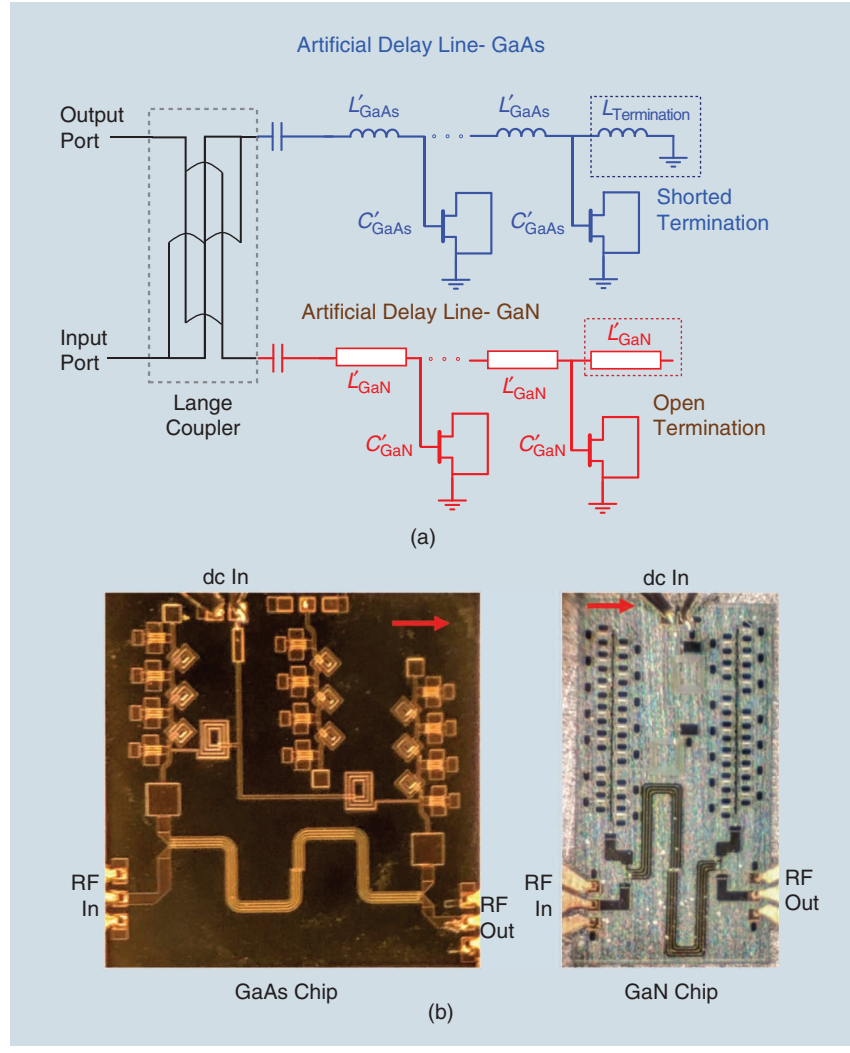

Figure 2. *(a) A topology of reflective loaded-line continuous broadband phase shifter. The coupled and through ports of the Lange coupler are variable reactances, as in a reflective phase shifter, implemented with tunable artificial transmission lines that use diode-connected transistors as variable capacitors. (b) 2.5 mm × 2.5 mm GaAs and 1 mm × 2.5 mm GaN MMIC phase shifter. Both reactive loads are implemented with lumped inductors and a shorted termination in the GaAs MMIC (in blue) and with transmission-line sections and an open termination in the GaN MMIC (in red). The gate directions for the chips are indicated with red arrows. The effects of bends in the Lange couplers are compensated with electrical length and bridge placement.*

Lange couplers and three lumped 0.4-nH inductors and four transistors in each shorted loaded line. For the D-mode GaN devices at 9 GHz, with a gate bias range of –3 to –1 V, the capacitance variation is 0.163–0.281 pF. The GaN phase shifter loaded lines are open-circuited and use 14 transistors with electrically short (1.7° at 12 GHz) high-impedance (95 Ω) lines as series inductors.

Figure 3(a) shows measured phase as a function of bias for the two MMICs in small-signal operation. Over this range, both phase shifters are matched with a return loss better than 10 dB across the frequency range, as a result of the reflective circuit architecture. The insertion loss is between 3 and 7 dB across the frequency range, based on tuning level. The MMICs are also tested for increased input power levels (5–25 dBm),

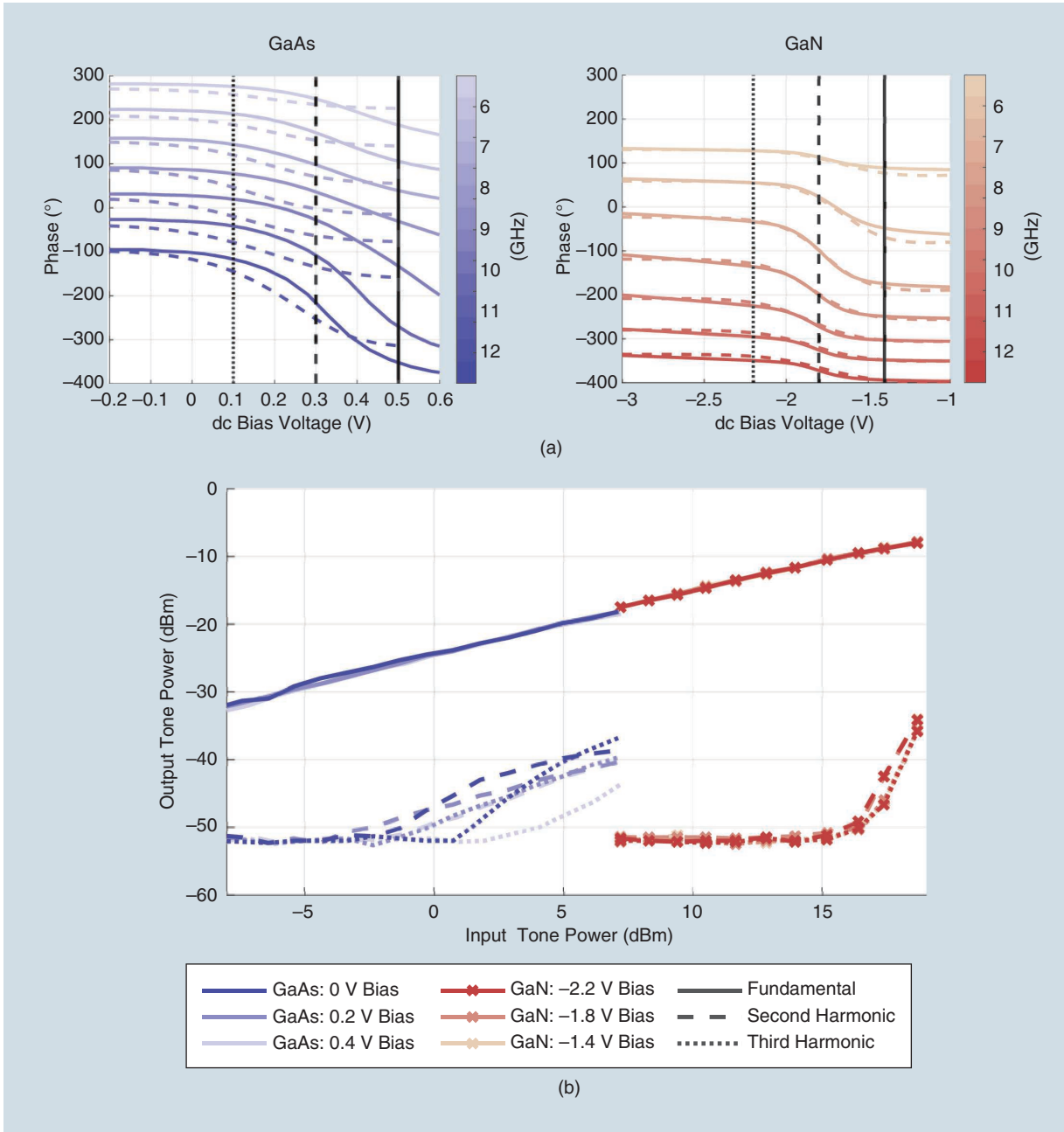

Figure 3. *(a) A measured and simulated phase as a function of gate bias for several frequencies. The black lines indicate lower (dotted) and upper (solid) biases for a useful voltage range. The results for the GaAs and GaN MMICs are shown on the left (in blue) and right (in red), respectively. Simulations are shown in dashed and measurements in solid line. (b) Harmonic generation as a function of input power for the GaAs (in blue) and GaN (in red) phase shifters at 9 GHz. At the low-power end, the measurements are limited by the sensitivity in the experimental setup.*

to evaluate the power handling and nonlinearities. A frequency-dependent increase in loss and a reduction in phase change is observed for both MMICs, but at different power levels, as expected. The GaAs MMIC, above 10 dBm of input power, provides 50°–60° of phase shift but with increasing loss. The GaN MMIC has 20°–75° of phase shift for up to 20 dBm of input power with little variation in $|S_{21}|$ compared to the small-signal case. The power dependence eventually levels because the first diode behaves as a short and the phase is no longer tunable. Figure 3(b) summarizes second and third harmonic generation behavior, showing that the GaN device is linear at 20-dB higher input power as compared to the GaAs device. This is expected and has benefits when higher drive power is needed for the final amplifier chain and nonlinearities in the phase shifter can affect the overall linearity.

In a phased array, the broadband phase shifters require integration in a broadband corporate feed network. A single-stage two-way Wilkinson power divider with a voltage standing-wave ratio (VSWR) of 2:1 has a 3:1 bandwidth. To increase the bandwidth further, multisection Wilkinson dividers can be implemented [36]. Air-based TEM waveguides offer lower loss and dispersion when compared to planar transmission lines such as microstrip [37]. Figure 4 shows a five-section greater than decade (11:1) bandwidth Wilkinson divider implemented in air-filled coaxial lines fabricated using the PolyStrata process, which involves sequential deposition of copper layers and photoresist on a silicon wafer [38]. The copper layer thicknesses range from 10 to 100 μm with aspect ratios larger than 1.5. After the desired layers are deposited, the photoresist is released leaving an air-filled low-loss structure, enabling low-loss air-filled coaxial lines up to W-band and waveguides at higher frequencies. The Wilkinson divider is measured with thru-reflect-line microcoaxial calibration and shows better than –13 dB match with a loss of 0.4–1.2 dB from 2 to 22 GHz [39]. Integration of a MMIC in the microcoaxial PolyStrata environment is demonstrated in [40], showing that MMIC phase shifters can be integrated in such a low-loss broadband beamforming network.

Broadband Butler Matrix

A Butler matrix, first reported in [41], is a network implemented with hybrid couplers and fixed phase shifters, as shown in Figure 5(a). The network has 2^N inputs and 2^N outputs, where N is the size of the matrix. Depending on which input is excited, a different phase progression is seen at the output antenna ports, corresponding to beams in different directions. For a 4×4 Butler matrix shown in the figure, two 90° coupler pairs

A broadband Butler matrix requires a low-reflection, low-loss, and high-isolation four-port crossover across a large bandwidth, not readily available in standard technologies.

(one at the input and one at the output) with 45° phase shifts in two of the branches and two crossovers, produce an output phase progression of ±45°, ±135°. A broadband Butler matrix requires a low-reflection, low-loss, and high-isolation four-port crossover across a large bandwidth, not readily available in standard technologies. The coupler amplitude and phase balance is critical since these errors are cascaded through the two coupler paths, and a fixed phased shifter across a wide bandwidth also requires careful design.

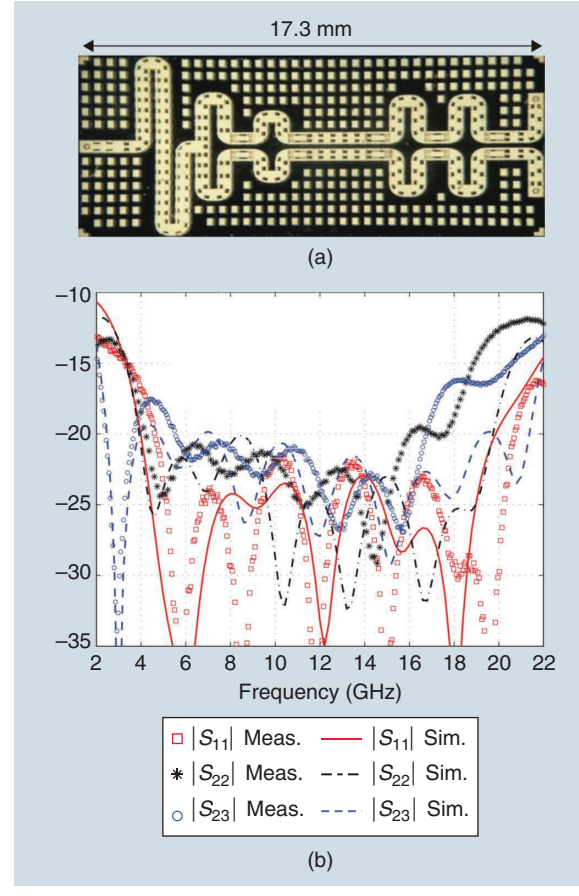

Figure 4. *A (a) photograph and (b) measured and full-wave simulated performance of a microcoaxial 2- to 22-GHz Wilkinson divider, which can be integrated with MMIC phase shifters into a low-loss broadband beamforming network. The device in the photo does not have mounted resistors. "Sockets" for mounting 0303 surface mount resistors are clearly visible and described in [39]. Meas.: measured; Sim.: simulated.*

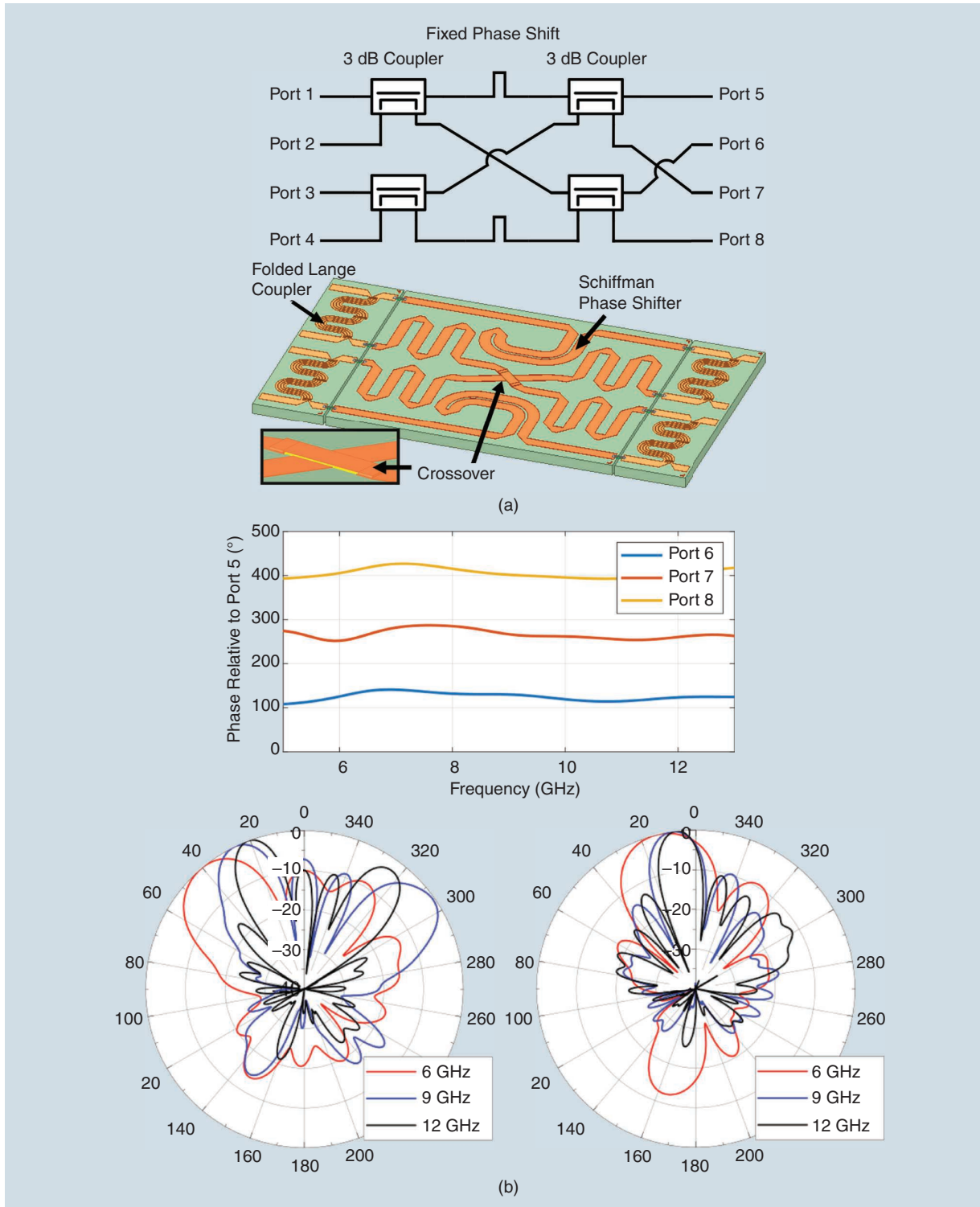

Figure 5. *(a) A schematic of a 4 × 4 Butler matrix with 90° hybrids. Under the matrix is an implementation in the HRL MECA heterogeneous integration process with alumina passives. Note that another crossover is necessary at the output for connection to the antenna array. The insert shows a closeup of the crossover, which utilizes the additional dimension given by the interconnect layer in the MECA process. (b) A full-wave simulated phase difference to the output ports when Port 1 is excited and all other ports terminated, with Port 5 serving as a reference for the phase, showing approximately 135° of phase progression. Under this is a far-field normalized H-plane radiation patterns of the Butler matrix feeding a broadband ridged horn antenna array when Port 1 (shown on the left) and Port 2 (shown on the right) are excited. Patterns are shown at the edge and middle of the band at 6 GHz (in red), 9 GHz (in blue), and 12 GHz (in black).*

Broadband 4 × 4 Butler matrices in the approximate frequency range of interest are summarized in Table 1 and include a 3- to 10-GHz multilayer stripline in [42] where the ports are not arranged for direct connection to an antenna array, the phase varies ±14° and insertion loss degrades severely at higher frequencies. In [43], a corrugated slot-coupled structure was used for the broadband components from 3.1 to 10.6 GHz, with a resulting magnitude and phase variation of ±1.2 dB and ±4.5°. A 1.8- to 12-GHz stripline design using multisection couplers is shown in [44] with the magnitude and phase variation between the ports of ±2 dB and phase ±15°. More narrowband versions with good performance are shown in SIW, e.g., from 8.5 to 10.6 GHz [45]. A larger 8 × 8 matrix from 2 to 18 GHz is shown in [48], with increased loss and amplitude/phase variation, especially at higher frequencies.

The design in Figure 5(a) is implemented in HRL's Laboratories metal embedded chip assembly (MECA) process [49], with broadband coupler and interconnects demonstrated in [50]. The goal of the design shown here is to minimize phase and amplitude imbalance over 6–12 GHz. The Lange couplers are folded to reduce footprint, the crossover and Schiffman fixed phase shifters are designed in the MECA interconnect layer, and additional delay lines provide the proper 45° difference between the middle and outer paths. This Butler matrix is designed in three separate pieces of alumina connected by broadband interconnects of the MECA process. Full-wave simulations are shown in Figure 5 for the phase progression referenced to Port 5 across the 6- to 12-GHz bandwidth with less than ±21° variation. In this range, the input ports are matched to better than 7 dB and the insertion loss is within 1.5 dB. Return loss is better than 10 dB above 7 GHz. This design would need another crossover between the inner two ports for connection to a 4 × 1 antenna array. Simulations with the antenna array made of broadband ridged horn antenna elements [51] result in radiation patterns shown in Figure 5(b). With Port 1 excited, which has phase progression of approximately 135°, at 6 GHz the beam steers 40°, while at 9 and 12 GHz the steering is 26° and 21°, respectively. With the phase progression corresponding to Port 2 of approximately 45°, at 6 GHz the beam steers by 14°, while at 9 GHz and 12 GHz a steering of 9° and 7° is obtained. This beamformer is currently being fabricated and will be connected to the antenna array described in the "Analysis of PAs in a Phased Array Environment" section.

The phase of each element is determined by the length of the feed line section between the elements as well as the mutual coupling.

Broadband Frequency Scanning

For space applications such as planetary-landing radar [52], higher millimeter-wave frequencies offer reduced mass but may not suffer attenuation as in the Earth's atmosphere. At W-band and above, MMIC phase shifters, e.g., [53], and Butler matrices, e.g., [54], become very lossy and require specialized technologies. Another approach is frequency steering, which requires a voltage-controlled oscillator and potentially also a frequency multiplier, possible in MMIC technologies. Frequency-scanned waveguide arrays have been used since the 1940s, e.g., [55], and require broadband components to achieve a large scan angle. Figure 6(a) shows a linear array where the elements are fed with a varying frequency, which changes the relative phase between elements resulting in beam steering. The input wave travels along the feed line and loses power at each element to radiation. Elements closer to the feed input couple weakly to the feed line, while elements near the load couple strongly and any remaining power after the last element is dissipated in the load (typically 10–15% of the input power). The phase of each element is determined by the length of the feed line section between the elements as well as the mutual coupling. In Figure 6(a) the array is fed by a line of physical length α between elements and propagation constant β, with element spacing of d in air. For an angle θ_m of the m-th beam

TABLE 1. Summary of broadband Butler matrices.

Reference	f_l (GHz)	f_h (GHz)	Technology	Size	$\Delta\theta$ (°)	ΔA (dB)
[42]	3	10	Stripline	4 × 4	14	Not given
[43]	3.1	10.6	Corrugated slot	4 × 4	4.5	1.2
[44]	1.8	12	Stripline	4 × 4	15	2
[45]	8.5	10.6	SIW	4 × 4	5	0.6
[46]	2	3	Stripline	4 × 4	3	Not given
[47]	8	12	Stripline	8 × 8	15	1
[48]	2	18	Stripline	8 × 8	15	1.5

peak, the phase is given by $\sin\theta_m = (\lambda_0/d)(\alpha/\lambda_g - m)$, where λ_0 and λ_g are the free-space and feed guided wavelength, respectively. Both a longer feed line section and a more dispersive delay line result in a wider beam scan with frequency.

Two W-band and G-band architectures, based on microcoaxial line fed slots and slotted waveguides, are introduced in [56]–[59]. The devices are fabricated using the PolyStrata process with coaxial lines at W-band, or at higher frequencies using lower-loss rectangular waveguides, which are comparable in size to the microcoax, but have higher dispersion and lower loss. An example 20-element linear waveguide-fed slot array, which scans from –40° to 0° when the frequency varies from 130 to 180 GHz is shown in Figure 6(b), along with measured radiation patters. This corresponds to approximately 1°/GHz of scanning with gain and scan angle over frequency shown in Figure 6(c). With the same approach and by introducing corrugations in the bottom waveguide feed wall, the dispersion is increased to achieve 2°/GHz in a 32 × 32 2D array with 1D scanning [59].

Isolation Circuits

Phased arrays are usually used to both transmit and receive, in which case some isolation method is required to protect the low-noise amplifier from saturating due to leakage from the transmitter. For nonsimultaneous transmit and receive applications, switches can have high isolation and transmitter

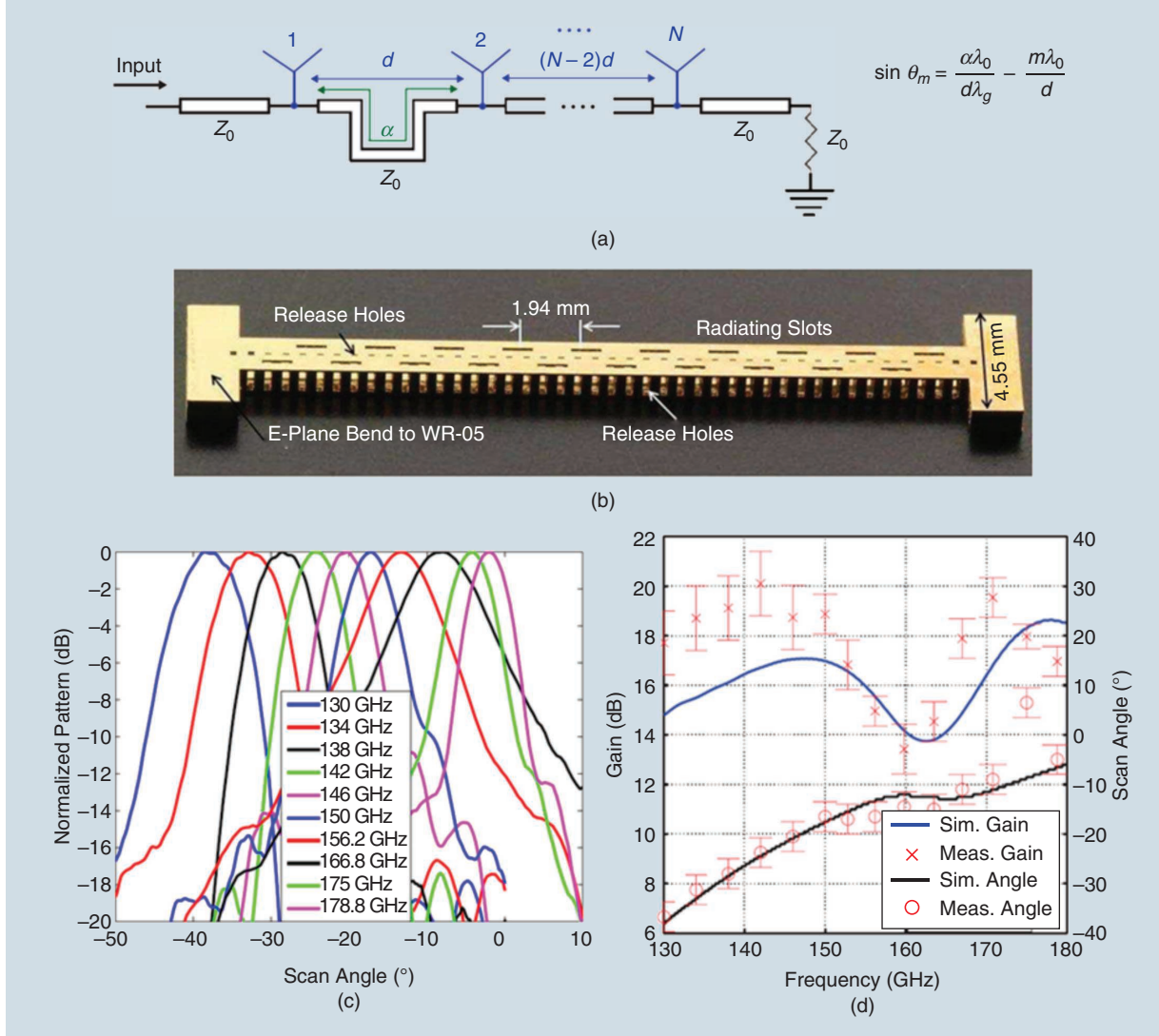

Figure 6. *(a) The principle of operation of frequency-scanned arrays where the phase at each radiating element depends on element spacing and dispersion of the feed line. (b) A microfabricated 20-element Polystrata WR-5 waveguide slotted array. (c) Measured normalized radiation patterns from 130 to 180 GHz and measured and simulated scan angle and gain over the frequency range [57].*

amplifier bias can be turned off during receive mode. For simultaneous transmit and receive, circulators or diplexers are used, depending on the frequency of the up/down links. Often the required levels of isolation are greater than 100 dB and exceed what can be done by only one method, so several methods including e.g., antenna polarization are added, and have been demonstrated over a wide bandwidth, e.g., [60]. At the circuit level, circulators are bulky and usually narrowband, so a MMIC solution is attractive. For self-interference and other cancellation over a wide bandwidth, tunable notch filters are useful but are large and the additional loss degrades the noise figure. An active analog canceler amenable to monolithic integration can also produce a tunable spectral notch over a wide bandwidth. Circulator and analog cancellation GaAs MMICs that operate over an octave bandwidth are presented next.

Active Circulator MMIC

Nonreciprocal behavior of transistors can be used to achieve circulation and was first presented in 1965 [61]. Later, a variety of architectures were further explored, e.g., [62]. In [63], a MMIC implementation using Qorvo's 0.25 μm GaAs pHEMT process, designed to operate in the 7–13 GHz band, is demonstrated (Figure 7). Circulation is accomplished by connecting three unconditionally stable, gain-matched, single-stage equal amplifiers with three asymmetric Lange couplers. The through ports are connected to the amplifier inputs, and the coupled ports to the outputs. The isolated ports are terminated in 50-Ω resistors and the Lange coupling coefficient specified to achieve a tradeoff between backward isolation ($|S_{31}|$) and forward gain ($|S_{21}|$), while ensuring stability. The forward gain of the circulator is proportional to the amplifier gain, reduced by the *coupling* and *through* attenuation of the

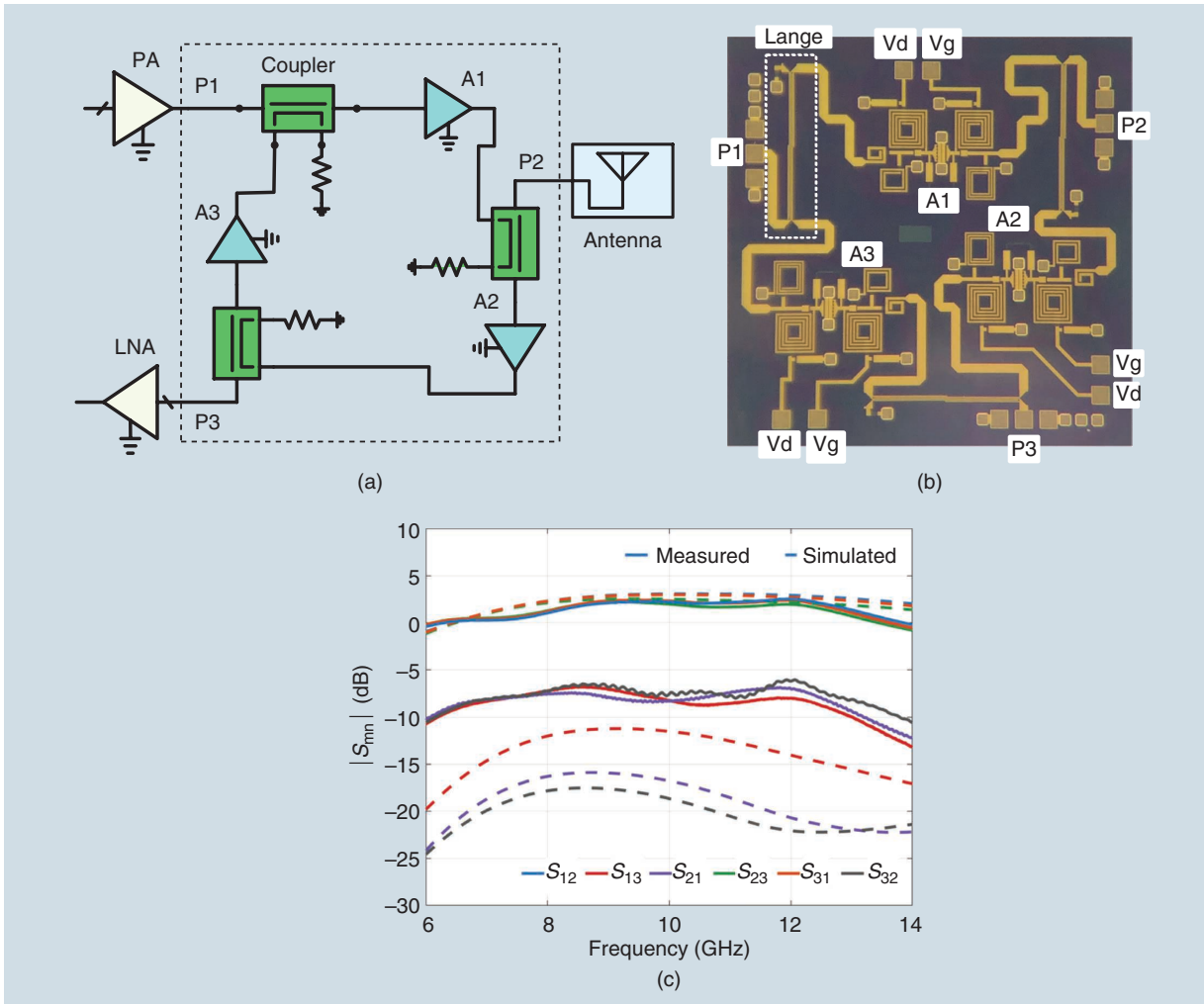

Figure 7. *(a) A broadband 7- to 13-GHz active circulator topology. (b) A photograph of an active circulator GaAs MMIC circuit. When Port 1 (P1) is the input, P2 is the output, and P3 isolated. (c) Simulated and measured results for 50-Ω loads at all ports from 6 to 14 GHz showing insertion gain of up to 2.4 dB with isolation $|S_{31}|$ greater than 13 dB across the band [63].*

Lange couplers. The simulated versus measured performance is shown in Figure 7(c). Simulations for 50-Ω loads at the ports shows insertion gain of up to 3 dB across 6–14 GHz with isolation $|S_{31}|$ greater than 13 dB. Measurements show good comparison to simulated insertion gain, but a decrease in isolation, explained later in this article.

The 2.5 mm × 2.5 mm chip [Figure 7(b)] behavior is analyzed when integrated in a phased array–like environment, where the port impedances vary and where process variations impact device performance [Figure 8(a)]. The circuit architecture contains many possible feedback paths, so stability needs to be carefully analyzed. Assuming that all port impedances can vary within a VSWR = 2, Figure 8(b) shows simulated statistical analysis of the loop gain for the three amplifiers in the circulator. A safe phase margin is obtained from dc to 20 GHz, indicating stability over a wide range of loads. To explain the degradation in isolation measured in Figure 7(c), a statistical analysis is performed with information provided by Qorvo for the GaAs process variations, and with additional load mismatch on all three ports inside the VSWR = 1.1 circle with a normal distribution of impedances. The results in Figure 8(c) show a large spread in the three isolation parameters. For some values of process parameters and load impedances, the degradation in isolation seen in the measurement is predicted.

Active Broadband Interference Cancellation

Agile broadband receivers are susceptible to self or external interference where the analog to digital converter (ADC) can become overloaded. A possible solution is the use of electronically-tunable passive filters, extensively reported in the literature, e.g., [64]–[66], however they can be lossy and bulky. Another solution is a cancellation circuit amenable to MMIC integration and cointegration with other front-end RF circuits. One

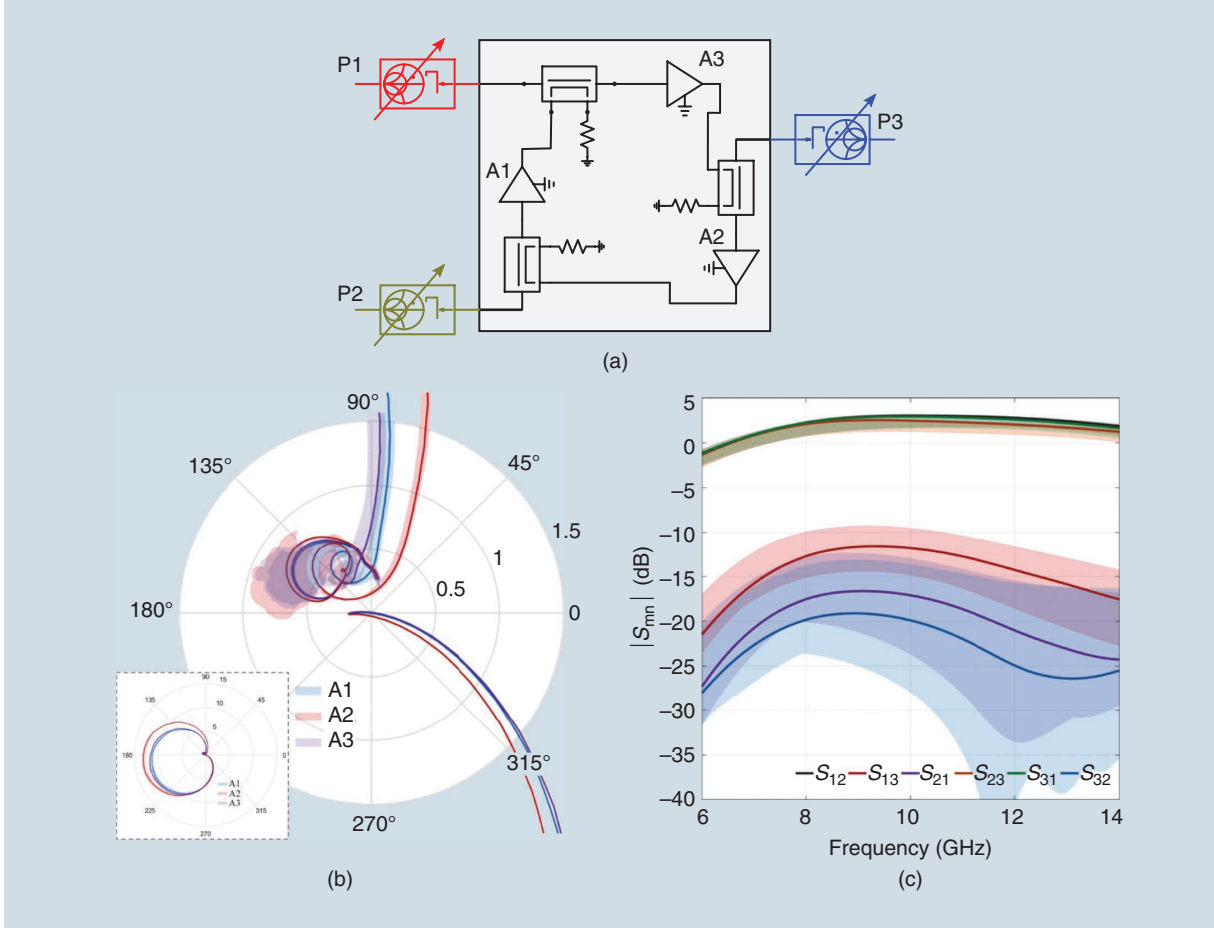

Figure 8. *A statistical analysis of stability, gain, and isolation on all three ports considering process and load variation. (a) A simulated loop gain for the three amplifiers (A1, A2, A3) when ports are terminated with loads within the VSWR = 2 circle, from dc to 20 GHz. (b) Gain and isolation on all three ports with process variation and loads within a VSWR = 1.1 circle. (c) A comparison between nominal design simulations and measurements when statistical variation is taken into account. The shaded bands show the range of parameters obtained with a normal distribution for impedance values.*

example is analog finite impulse response filters, which have been implemented in CMOS and GaAs and used as equalizers in optical communication systems [67]–[69]. A similar idea has been used in RFID for leaking carrier suppression, where an interferometer circuit is designed for the carrier signal [70]. Here we extend these ideas to an active circuit that applies vector addition to eliminate unwanted signals, while relying on a single input signal.

The general interferometer circuit topology shown in Figure 9(a) creates tunable spectrum notches that can be placed over the largest interferers to reduce the dynamic range requirements on the ADC. The Lange couplers divide and recombine the input signal; one path has only a gain stage, while the other path also includes a variable lumped-element transmission line with variable shunt capacitances. In an MMIC, these are implemented with gate-source grounded transistors, which act as varactors. By changing the bias on the transistors, the delay through the artificial transmission line is varied to achieve destructive interference between the two paths at a given frequency. The MMIC shown in Figure 9(b) is designed in the WIN Semiconductors' GaAs E-mode single-polarity supply PIH10 process to operate across X-band. The two gain stages are biased slightly different with more gate voltage applied to the path with the transmission line to account for the additional loss. Figure 9(c) shows measured behavior when the control voltage for the variable transmission line varies from −0.7 V to 0.7 V. The circuit is well matched from 6 GHz to 12 GHz, while the null can be moved from 8.2 GHz to 10.8 GHz. The measured behavior matches the simulated behavior, except for a 0.4 GHz downward shift in tuning range frequency.

Analysis of PAs in a Phased-Array Environment

In transmit phased array, e.g., for jamming applications, PAs are the last active component in the chain preceding the antenna elements. This section presents an analysis of such a chain, noting that the effects of a switch, circulator, or diplexer can be added without loss of generality. Figures-of-merit (FoM) for broadband transmit electronically scanned arrays are highly dependent on both passive and active component variation over frequency and power as well as their interactions. The FoMs we consider here are related to the circuit side of the array, and include impedance variation due to antenna coupling, power-added and overall efficiency, and gain/loss. The antenna-related FoMs are the EIRP and scan volume, not discussed here. We first consider how the coupling between elements affects the PA efficiency, on the example of a small horn antenna presented in [51] and shown in Figure 10(a) and (b) together with its measured and simulated octave-bandwidth performance. This antenna element is characterized, built into a 4×1 linear array [Figure 10(c)] and is a starting point for analyzing effects of impedance variation on the PAs that feed the four ports in the active array.

Figure 11(a) shows the block diagram used in simulation for coupling analysis as a function of the scan angle assuming ideal phase shifters. The full-wave electromagnetic (EM) simulations (HFSS) are imported into Cadence/AWR Microwave Office circuit simulations to determine the coupling as a function of progressive phase shift across the array. A coupler in each element is used to measure the complex backward propagating wave from the antenna through the phase shifter. The power of this wave in

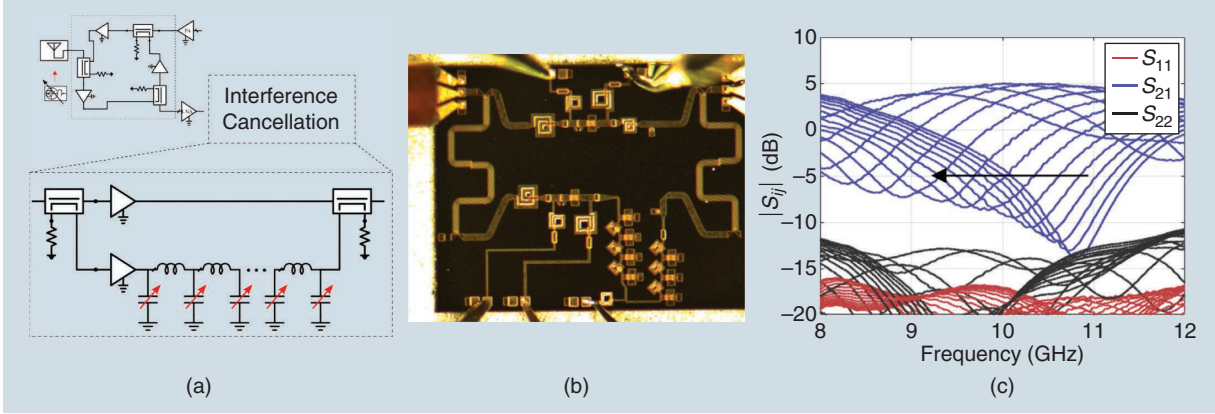

Figure 9. *(a) A block diagram of the active broadband interference cancellation MMIC. (b) A photograph of fabricated GaAs MMIC. (c) Measured amplitude of transmission and reflection coefficients with variation of the control voltage on the variable-delay artificial transmission line. The drain bias on both paths is 2 V and the gate bias on the upper and lower paths is 0.8 V and 1 V, respectively. As the control voltage increases from −0.7 V to 0.7 V, the notch created by the destructive interference moves down in frequency from 10.8 GHz to 8.2 GHz, as shown by the arrow.*

each port, when all other ports are fed with a nominal 0 dBm of input power, is shown in Figure 11(b) across frequency. As expected, the two inner and two outer elements show symmetric behavior. The ratio of the complex reflected wave and the incident wave gives the reflection coefficient, and therefore impedance presented to each amplifier when the other ports are active.

The PA used for the analysis is a 6- to 12-GHz Qorvo QPA2598 GaN MMIC die, with a peak output power of 2 W, small-signal gain of 23 dB and power-added efficiency (PAE) = 30% in continuous wave (CW) operation at a drain bias of 25 V. Qorvo provided an X-parameter model for this device, with simulated large-signal parameters shown in Figure 12. The coupling between the output ports of the PAs, associated with a progressive phase shift for different steering angles, forces active impedance trajectories shown in the Smith charts in Figure 13 for the edges and center of the octave band, and given by

$$\Gamma_{1,\text{active}} = \frac{b_1}{a_1} = S_{11} + S_{12}\frac{b_2}{a_1} + S_{13}\frac{b_3}{a_1} + S_{14}\frac{b_4}{a_1}.$$

The simulation setup is shown in Figure 13(a), and the active impedance coupling matrix as a function of progressive phase shift for $\phi = [-180°, 180°]$ computation [Figure 13(b)] is used to evaluate the PAE load-pull performance of the linear active array at 1 dB compression of each of the PAs. Note that the maximum PAE is obtained for different impedances across the bandwidth, ranging from close to 50 Ω at 6 GHz to an inductive impedance at 9 GHz and a lower real impedance at 12 GHz. The design attempted a flat PAE at 50 Ω and over frequency. In a 4 × 1 array, outer and inner elements have the

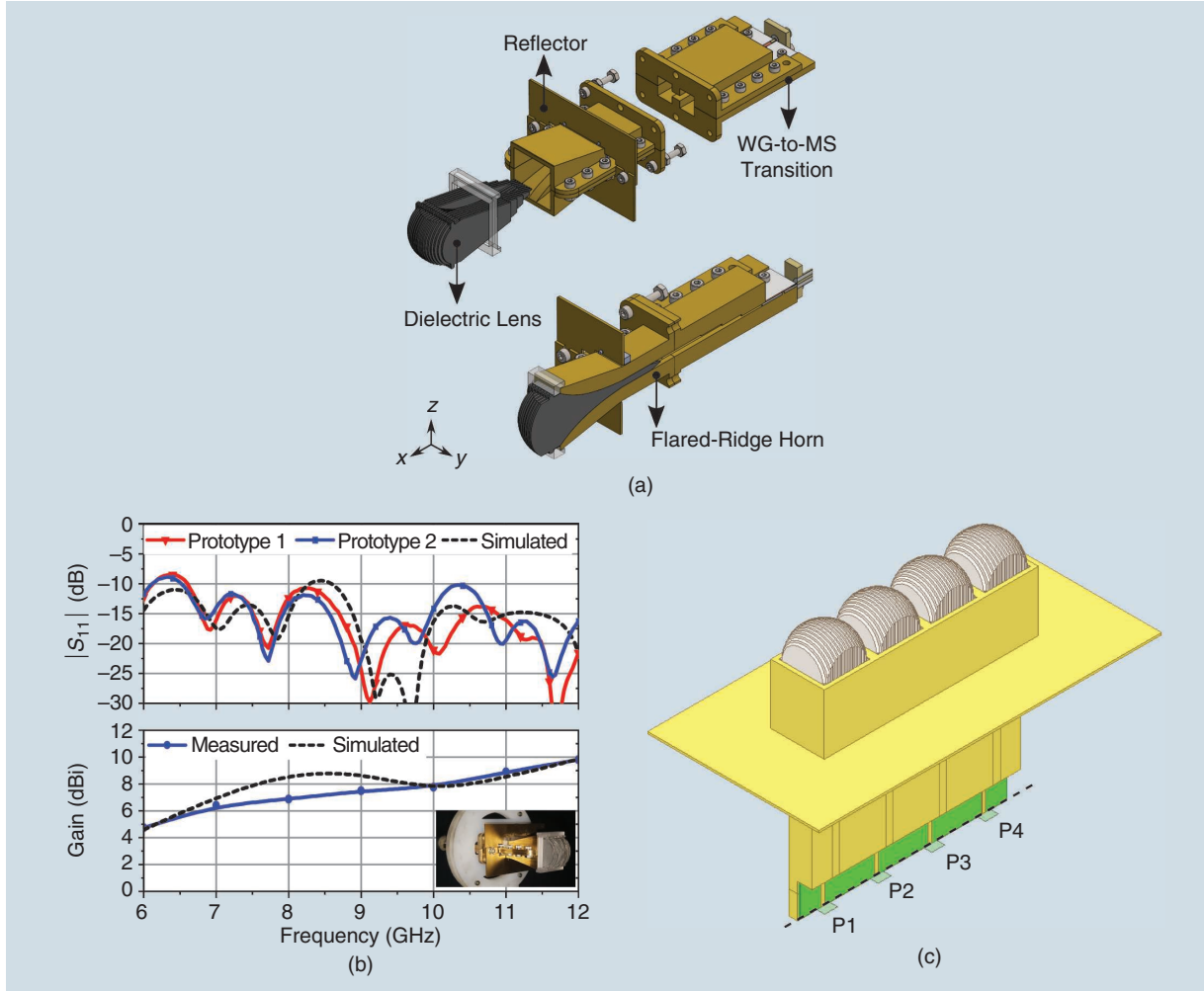

Figure 10. *(a) An octave-bandwidth small-aperture ridge waveguide horn with dielectric lens showing the waveguide-to-microstrip transition [71], E-plane ridge, and dielectric loading that improves the match. (b) A measured and simulated return loss and gain from 6 to 12 GHz [51]. (c) The horn elements are combined in a 4 × 1 linear active array with broadband GaN MMIC PAs feeding ports P1–P4.*

same Γ trajectory behavior, but occupy symmetric loci in each path, so the PAE and P_{Out} performance is different for each element [Figure 13(c)]. The PAE of the four amplifiers as a function of progressive phase shift $\phi = [-60°, +60°]$ is shown in Figure 14 across frequency.

Discussion and Outlook

Broadband phased array implementations present numerous challenges, and this article only touches upon some front-end components that offer performance over octave or larger bandwidth in the microwave and millimeter-wave ranges. There are a number of other useful advances in the areas of array calibration and high-efficiency PAs with dynamic supplies, briefly overviewed next.

Sensors for Electric Field Measurements

Calibration of phased arrays often involves measurements of near-field magnitude and phase across the aperture, e.g., [72] and [73]. Recent interest in quantum sensors for microwave electrometry have resulted in a number of demonstrations of both room-temperature [74]–[76] and cold [77] Rydberg-atom field measurements. These alkali atoms in highly excited states can be used to make traceable microwave electric field

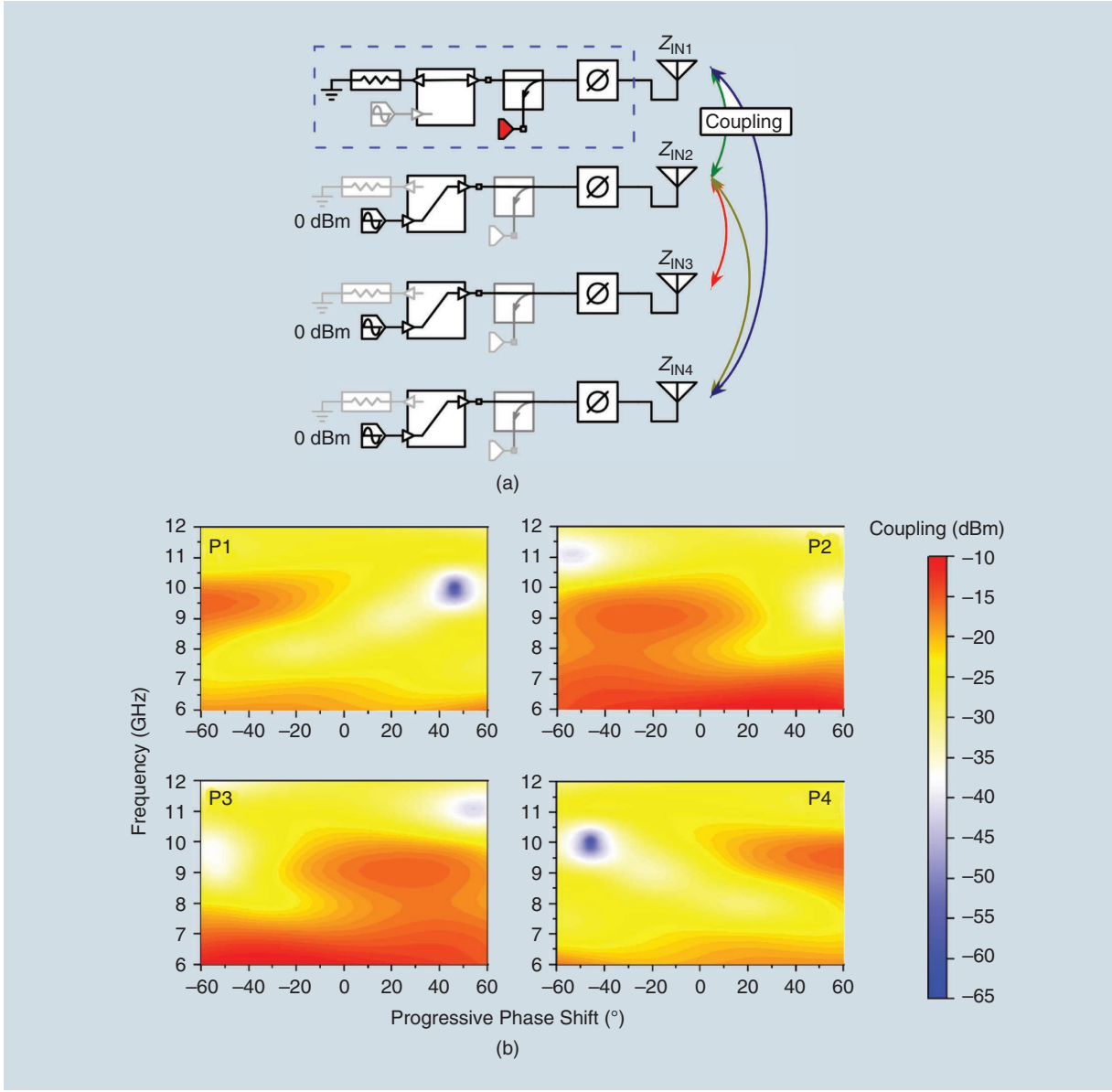

Figure 11. *(a) Simulation setup where the full-wave EM simulated 4-element linear array is imported into a circuit simulation with ideal phase shifters, couplers, and switches to determine coupling between elements. (b) Simulated coupling over frequency and progressive phase shift for the four elements of the array at ports P1–P4 indicated in Figure 10(c).*

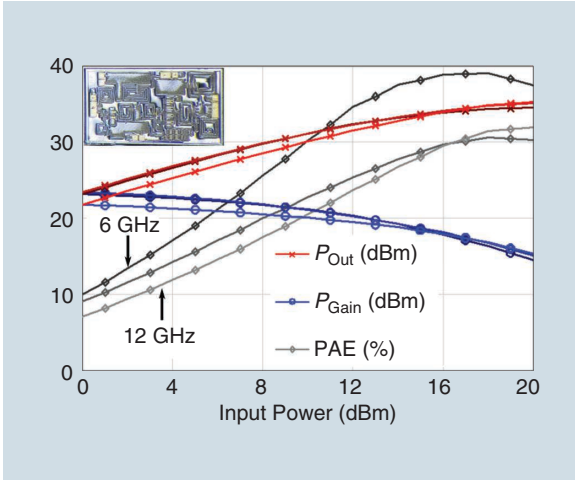

Figure 12. *Output power, power gain, and PAE for the 2-W Qorvo QPA2598 GaN MMIC PA, simulated with an available X-parameter model obtained from measurements. The simulation conditions are at a drain voltage V_{dd} = 25V V and with 50-Ω port terminations.*

measurements and require a calibration factor as shown in [74]. The atoms in a vapor cell are excited with two lasers ("coupling" and "probe") at specific wavelengths making them sensitive to specific microwave frequencies. In principle, with widely tunable laser wavelengths, a practically continuous bandwidth from low GHz to millimeter-waves can be sensed. Rydberg atoms potentially increase sensitivity of electric field measurements over traditional probes and detectors down to 780 pV/m [78]. The electric field is extracted from a frequency measurement traceable to the fundamental Plank constant h as $|E| = (h\Delta f_m)/\rho$, where ρ is the dipole moment of the atomic transition, and Δf_m is the change in frequency of the spectral splitting (known as Autler-Townes splitting). A photograph of a room-temperature Rubidium Rydberg-atom vapor cell and electric field measurements derived from Autler-Towns splitting are shown in Figure 15. The cell is made of glass and can be made very small, while the spatial resolution of the electric field detector is determined by the size of

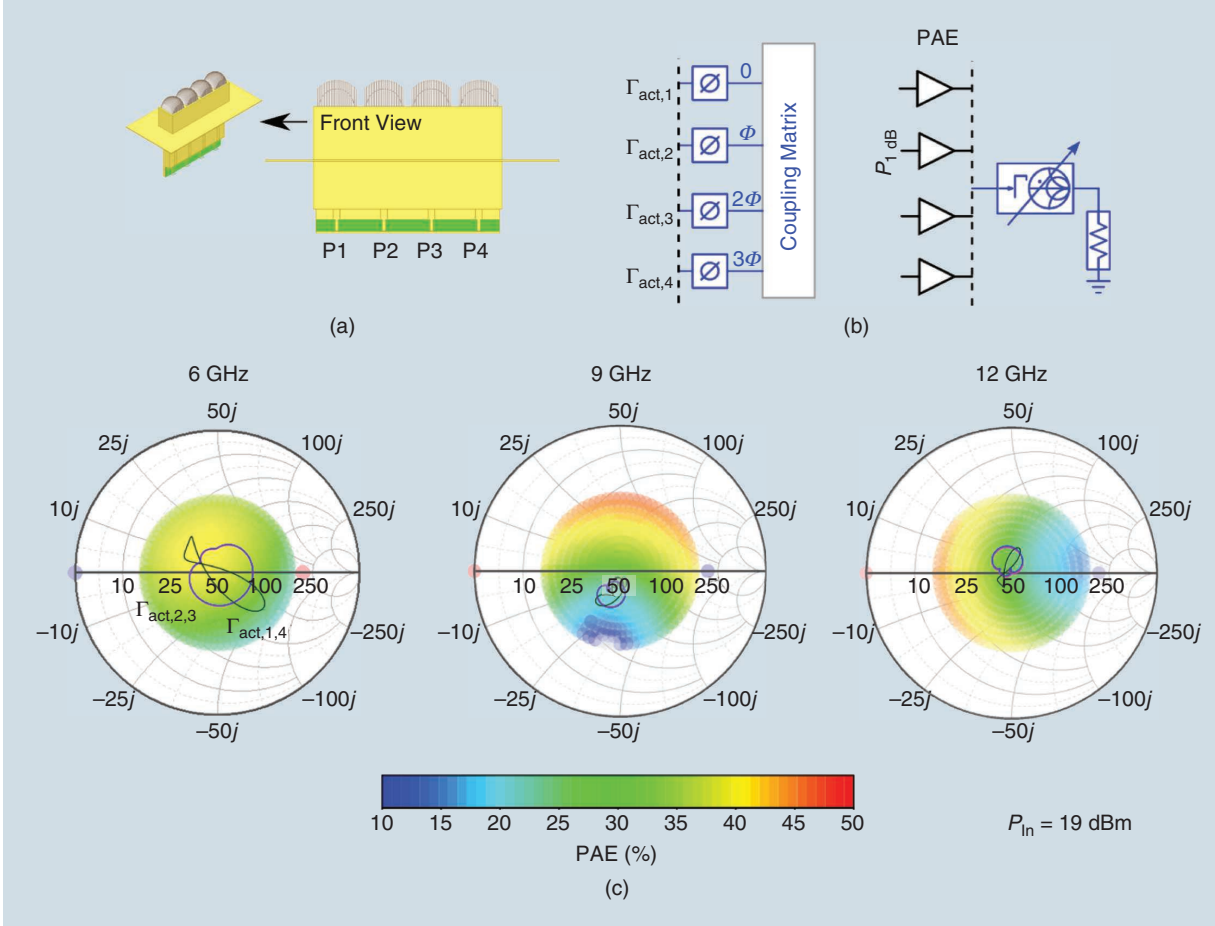

Figure 13. *(a) Array geometry used for computing the coupling matrix in HFSS. (b) Simulation schematics for active impedance computation as a function of progressive phase shift for ϕ = [–180°, 180°], and load-pull schematic for computing PA the PAE at 6, 9, and 12 GHz at 1 dB compression. (c) A Smith chart showing Γ_A trajectory of inner and outer elements overlapped with PAE shown in color.*

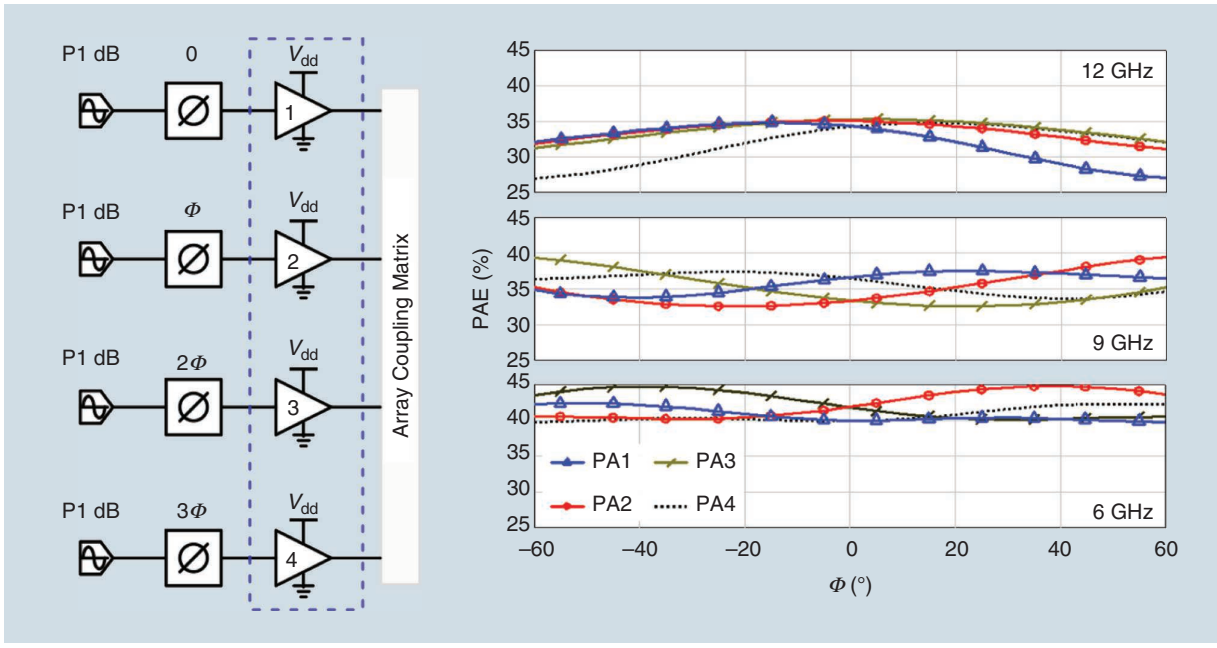

Figure 14. *PAE as a function of progressive phase shift across the 4-element linear array, across frequency and for all four amplifiers (PA1–PA4) driven 1 dB into compression.*

two intersecting laser beams. Recently demonstrated heterodyne measurements, e.g., [75] improve sensitivity and show potential of very sensitive electric field amplitude and phase measurements over a broad bandwidth.

Enhanced-Efficiency Broadband PAs

The PA used for simulations in the previous section is a commercial general-purpose broadband GaN MMIC with limited efficiency. PAs with enhanced efficiency through dynamic power supplies (envelope tracking [79]) have been demonstrated at higher power levels, with higher efficiencies and at increased frequencies. An example PA designed for K-band satellite communications from 18 to 25 GHz is described in [80]. This three-stage GaN MMIC fabricated in the Qorvo 150-nm process and shown in Figure 16(a) shows over 40% efficiency in CW with 4 W of output power from 18 to 24 GHz. The drain supply lines for the three stages can be accessed separately and by changing them dynamically with the envelope of a modulated signal, the average efficiency is improved. This approach of efficiency enhancement can be extended to high envelope bandwidths and multiple simultaneous signals over a large bandwidth.

Conclusions

This article presents several MMIC components amenable to heterogeneous integration for broadband-phased array, investigated by former and current Women in Microwaves students at the University of Colorado. GaAs and GaN octave-bandwidth 6–12-GHz MMIC phase shifters with a circuit topology that combines the reflective and loaded-line architectures are demonstrated for analog beamformers as well as a 6–12-GHz Butler matrix and a frequency-scanned broadband 130–180-GHz array. An active 6–14-GHz MMIC circulator is presented with potential of integration in GaN for increased power handling. For reducing unwanted interference, a GaAs MMIC with integrated low-noise amplifier can provide a broadband tunable notch in the 6–12-GHz range. Finally, the transmit portion of a four-element active array is analyzed to understand effects of element coupling on PAE over an octave bandwidth.

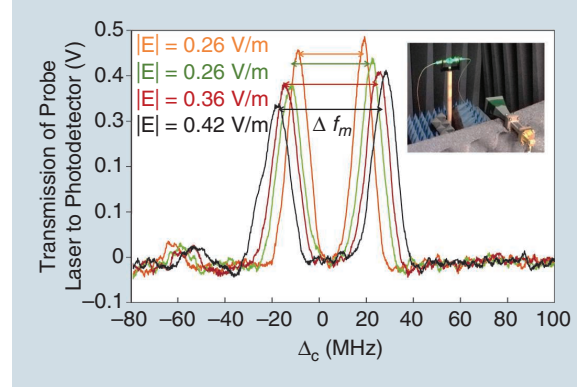

Figure 15. *An example of a measured electric field of a 17.04 GHz plane wave, copolarized with the light derived from Autler-Towns splitting measurements. The inset shows a photograph of Rubidium Rydberg-atom vapor cell made of Pyrex glass, with laser light input from fibers to excite a specific atomic transition corresponding to 17.04 GHz.*

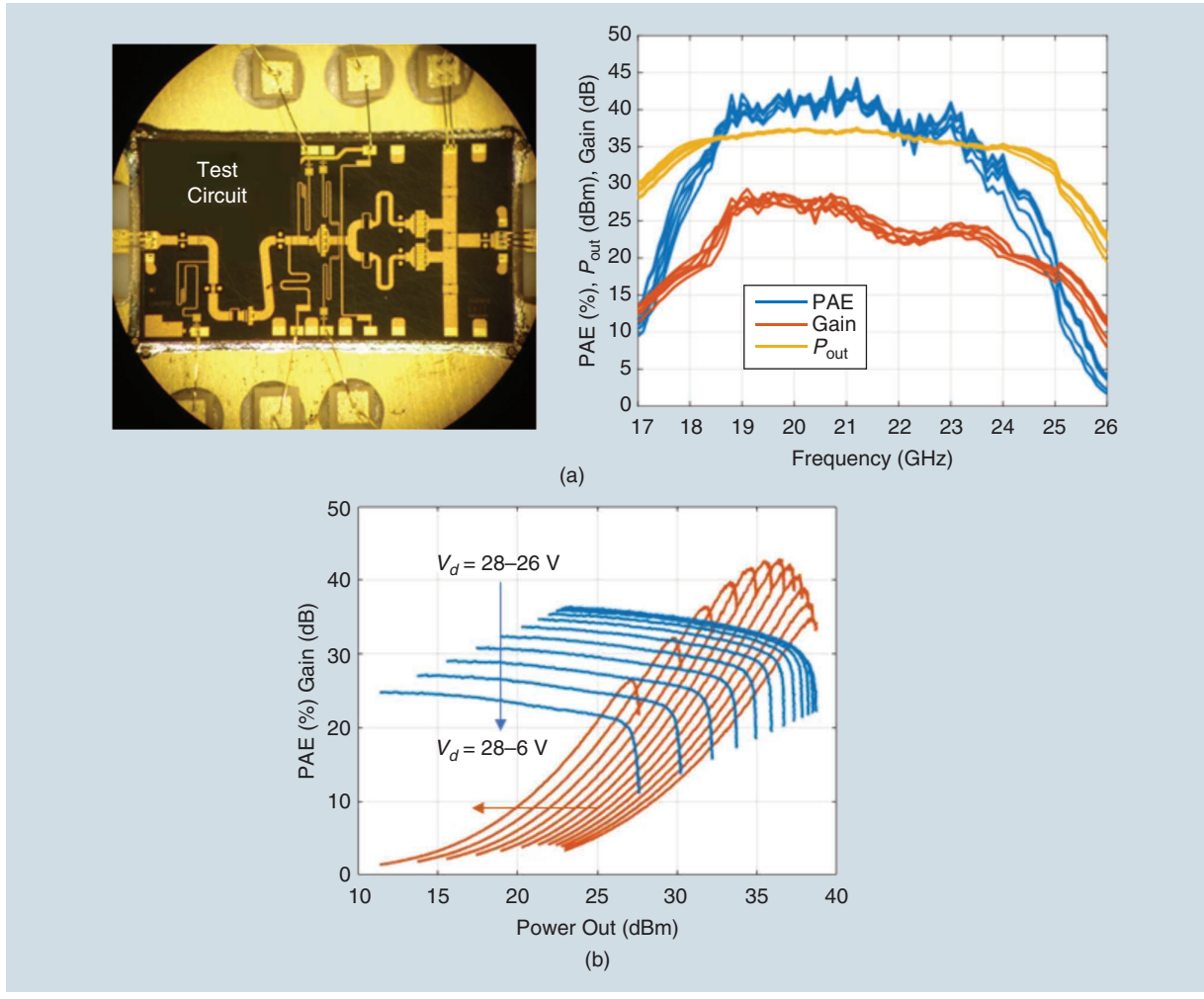

Figure 16. *(a) A photograph of a three-stage K-band GaN MMIC PA and measured large-signal CW performance for 10 packaged MMICs [80]. (b) Efficiency curves when the supplies of the last two stages of the PA are varied, moving the efficiency peak to different power (envelope) values and thereby increasing efficiency for modulated signals.*

Ongoing research at the University of Colorado includes Rydberg-atom electrometry aimed at traceable phased-array calibration as well as broadband MMIC PAs with supply modulation for efficiency enhancement for simultaneous signals transmitted on different beams.

Acknowledgments

We thank Qorvo and WIN Semiconductors for MMIC fabrication as a part of the ECEN 5014 Active Microwave Circuits class at the University of Colorado. We also thank Dr. S. Schafer at Qorvo for MMIC PA donation and X-parameter models, C. Hay at ADI for phase shifter donation and models, Cadence and Ansys for AWR and HFSS software donation, and J. Mologni at Ansys for assistance with the AWR–HFSS interface. We thank Prof. G. Lasser for many useful inputs. We are also grateful to Dr. J. Navarro at Boeing for helpful discussions related to antenna array performance metrics. This work was supported by ONR, the Department of Defense through a National Defense Science Engineering Graduate Fellowship (P. Danielson), Lockheed Martin, NIST, DARPA, JPL, and AFOSR. Zoya Popovic´ acknowledges support from a Lockheed Martin Endowed Chair of RF Engineering at the University of Colorado Boulder, and thanks her past and present graduate students of all genders for their hard work and dedication to the profession.

References

[1] K. Kibaroglu, M. Sayginer, T. Phelps, and G. M. Rebeiz, "A 64-element 28-GHz phased-array transceiver with 52-dBm EIRP and 8–12-Gb/s 5g link at 300 meters without any calibration," *IEEE Trans. Microw. Theory Techn.*, vol. 66, no. 12, pp. 5796–5811, 2018, doi: 10.1109/TMTT.2018.2854174.

[2] S. Shahramian, M. J. Holyoak, A. Singh, and Y. Baeyens, "A fully integrated 384-element, 16-tile, W-band phased array with self-alignment and self-test," *IEEE J. Solid-State Circuits*, vol. 54, no. 9, pp. 2419–2434, 2019, doi: 10.1109/JSSC.2019.2928694.

[3] Y. Kawaguchi, H. Nakagawa, S. Tanaka, and T. Yamada, "Application of phased-array antenna technology to the 21 GHz broadcasting satellite for rain-attenuation compensation," in *Proc. 2002 IEEE*

Int. Conf. Commun. Conf. ICC (Cat. No. 02CH37333), vol. 5, pp. 2962–2966, doi: 10.1109/ICC.2002.997383.

[4] E. Lier, J. Huffman, W. N. Kefauver, B. Dawley, and F. Butscher, "Satellite antenna capabilities pioneered at Lockheed Martin space systems company," in *Proc. 2017 IEEE 11th Eur. Conf. Antennas Propag. (EUCAP)*, pp. 1506–1510, doi: 10.23919/EuCAP.2017.7928455.

[5] H. Hommel and H.-P. Feldle, "Current status of airborne active phased array (AESA) radar systems and future trends," in *Proc. 2005 IEEE MTT-S Int. Microw. Symp. Dig.*, pp. 1449–1452, doi: 10.1109/MWSYM.2005.1516962.

[6] J. Schoebel et al., "Design considerations and technology assessment of phased-array antenna systems with RF MEMS for automotive radar applications," *IEEE Trans. Microw. Theory Techn.*, vol. 53, no. 6, pp. 1968–1975, 2005, doi: 10.1109/TMTT.2005.848838.

[7] M. Dudek, I. Nasr, G. Bozsik, M. Hamouda, D. Kissinger, and G. Fischer, "System analysis of a phased-array radar applying adaptive beam-control for future automotive safety applications," *IEEE Trans. Veh. Technol.*, vol. 64, no. 1, pp. 34–47, 2014, doi: 10.1109/TVT.2014.2321175.

[8] D. Zrnic et al., "Agile-beam phased array radar for weather observations," *Bull. Amer. Meterol. Soc.*, vol. 88, no. 11, pp. 1753–1766, 2007, doi: 10.1175/BAMS-88-11-1753.

[9] E. Yoshikawa et al., "MMSE beam forming on fast-scanning phased array weather radar," *IEEE Trans. Geosci. Remote Sens.*, vol. 51, no. 5, pp. 3077–3088, 2012, doi: 10.1109/TGRS.2012.2211607.

[10] R. Kronberger, T. Knie, R. Leonardi, U. Dettmar, M. Cremer, and S. Azzouzi, "UHF RFID localization system based on a phased array antenna," in *Proc. 2011 IEEE Int. Symp. Antennas Propag. (APSURSI)*, pp. 525–528, doi: 10.1109/APS.2011.5996761.

[11] K. F. Warnick, R. Maaskant, M. V. Ivashina, D. B. Davidson, and B. D. Jeffs, "High-sensitivity phased array receivers for radio astronomy," *Proc. IEEE*, vol. 104, no. 3, pp. 607–622, 2016, doi: 10.1109/JPROC.2015.2491886.

[12] S. W. Ellingson and G. A. Hampson, "A subspace-tracking approach to interference nulling for phased array-based radio telescopes," *IEEE Trans. Antennas Propag.*, vol. 50, no. 1, pp. 25–30, 2002, doi: 10.1109/8.992558.

[13] O. M. Bucci, L. Crocco, R. Scapaticci, and G. Bellizzi, "On the design of phased arrays for medical applications," *Proc. IEEE*, vol. 104, no. 3, pp. 633–648, 2016, doi: 10.1109/JPROC.2015.2504266.

[14] T. Hall et al., "Non-contact sensor for long-term continuous vital signs monitoring: A review on intelligent phased-array Doppler sensor design," *Sensors*, vol. 17, no. 11, p. 2632, 2017, doi: 10.3390/s17112632.

[15] J. Crezee et al., "Improving locoregional hyperthermia delivery using the 3-D controlled amc-8 phased array hyperthermia system: A preclinical study," *Int. J. Hyperthermia*, vol. 25, no. 7, pp. 581–592, 2009, doi: 10.3109/02656730903213374.

[16] M. Metcalf et al., "High-resolution phased-array MRI of the human brain at 7 tesla: Initial experience in multiple sclerosis patients," *J. Neuroimag.*, vol. 20, no. 2, pp. 141–147, 2010, doi: 10.1111/j.1552-6569.2008.00338.x.

[17] B. H. Waters, B. J. Mahoney, V. Ranganathan, and J. R. Smith, "Power delivery and leakage field control using an adaptive phased array wireless power system," *IEEE Trans. Power Electron.*, vol. 30, no. 11, pp. 6298–6309, 2015, doi: 10.1109/TPEL.2015.2406673.

[18] J. Navarro, "Affordable, multi-function flight-worthy airborne phased-array sensor," in *Proc. 2020 IEEE/MTT-S Int. Microw. Symp. (IMS)*, pp. 829–832, doi: 10.1109/IMS30576.2020.9224040.

[19] R. J. Mailloux, *Phased Array Antenna Handbook*. Norwood, MA, USA: Artech House, 1994, pp. 35–38.

[20] E. Brookner, "Advances and breakthroughs in radars and phased-arrays," in *Proc. 2016 IEEE CIE Int. Conf. Radar (RADAR)*, pp. 1–9, doi: 10.1109/RADAR.2016.8059284.

[21] A. Suriani, P. Capece, and G. Mannocchi, "Developments in SAR active phased array antennas in Thales Alenia space," in *Proc. 2019 IEEE Int. Symp. Phased Array Syst. Technol. (PAST)*, pp. 1–4, doi: 10.1109/PAST43306.2019.9020799.

[22] G. Kriehn et al., "Optical BEAMTAP beam-forming and jammer-nulling system for broadband phased-array antennas," *Appl. Opt.*, vol. 39, no. 2, pp. 212–230, 2000, doi: 10.1364/AO.39.000212.

[23] F. Hu and K. Mouthaan, "A 1–20 GHz 400 ps true-time delay with small delay error in 0.13 µm CMOS for broadband phased array antennas," in *Proc. 2015 IEEE MTT-S Int. Microw. Symp.*, pp. 1–3, doi: 10.1109/MWSYM.2015.7166834.

[24] C. Fulton, M. Yeary, D. Thompson, J. Lake, and A. Mitchell, "Digital phased arrays: Challenges and opportunities," *Proc. IEEE*, vol. 104, no. 3, pp. 487–503, 2016, doi: 10.1109/JPROC.2015.2501804.

[25] P. K. Bailleul, "A new era in elemental digital beamforming for spaceborne communications phased arrays," *Proc. IEEE*, vol. 104, no. 3, pp. 623–632, 2016, doi: 10.1109/JPROC.2015.2511661.

[26] J. S. Herd and M. D. Conway, "The evolution to modern phased array architectures," *Proc. IEEE*, vol. 104, no. 3, pp. 519–529, 2016, doi: 10.1109/JPROC.2015.2494879.

[27] R. C. Hansen, *Phased Array Antennas*. Hoboken, NJ, USA: Wiley, 2009, vol. 213, pp. 221–276.

[28] S. Barker and G. M. Rebeiz, "Distributed MEMS true-time delay phase shifters and wide-band switches," *IEEE Trans. Microw. Theory Techn.*, vol. 46, no. 11, pp. 1881–1890, 1998, doi: 10.1109/22.734503.

[29] X. Sun, J.-M. Fernández-González, M. Sierra-Pérez, and B. Galocha-Iragüen, "Low-loss loaded line phase shifter for radar application in X band," in *Proc. 2018 IEEE 15th Eur. Radar Conf. (EuRAD)*, pp. 477–480, doi: 10.23919/EuRAD.2018.8546574.

[30] E. G. Erker et al., "Monolithic Ka-band phase shifter using voltage tunable BaSrTiO3 parallel plate capacitors," *IEEE Microw. Guided Wave Lett.*, vol. 10, no. 1, pp. 10–12, 2000, doi: 10.1109/75.842071.

[31] J. J. Venter, T. Stander, and P. Ferrari, "X-band reflection-type phase shifters using coupled-line couplers on single-layer RF PCB," *IEEE Microw. Compon. Lett.*, vol. 28, no. 9, pp. 807–809, 2018, doi: 10.1109/LMWC.2018.2853562.

[32] A. N. Sychev, I. M. Dobush, N. Y. Rudyi, and S. M. Struchkov, "Analog phase shifter of X-band implemented with novel trans-directional coupled-line coupler," in *Proc. 2018 IEEE 48th Eur. Microw. Conf. (EuMC)*, pp. 811–814, doi: 10.23919/EuMC.2018.8541796.

[33] W.-T. Li, Y.-H. Kuo, Y.-M. Wu, J.-H. Cheng, T.-W. Huang, and J.-H. Tsai, "An X-band full-360° reflection type phase shifter with low insertion loss," in *Proc. 2012 IEEE 42nd Eur. Microw. Conf.*, pp. 1134–1137, doi: 10.23919/EuMC.2012.6459298.

[34] S. Lucyszyn and I. D. Robertson, "Two-octave bandwidth monolithic analog phase shifter," *IEEE Microw. Guided Wave Lett.*, vol. 2, no. 8, pp. 343–345, 1992, doi: 10.1109/75.153608.

[35] M. Robinson, P. Danielson, and Z. Popović, "Continuous broadband GaAs and GaN mmic phase shifters," *IEEE Microw. Compon. Lett.*, early access, 2021, doi: 10.1109/LMWC.2021.3115411.

[36] S. B. Cohn, "A class of broadband three-port TEM-mode hybrids," *IEEE Trans. Microw. Theory Techn.*, vol. 16, no. 2, pp. 110–116, 1968, doi: 10.1109/TMTT.1968.1126617.

[37] D. S. Filipovic, M. V. Lukic, Y. Lee, and D. L. Fontaine, "Monolithic rectangular coaxial lines and resonators with embedded dielectric support," *IEEE Microw. Compon. Lett.*, vol. 18, no. 11, pp. 740–742, 2008, doi: 10.1109/LMWC.2008.2005228.

[38] D. W. Sherrer and J. J. Fisher, "Coaxial waveguide microstructures having an active device and methods of formation thereof," U.S. Patent 7,148,772, Dec. 12, 2006.

[39] N. Ehsan, K. Vanhille, S. Rondineau, E. D. Cullens, and Z. B. Popovic, "Broadband micro-coaxial Wilkinson dividers," *IEEE Trans. Microw. Theory Techn.*, vol. 57, no. 11, pp. 2783–2789, 2009, doi: 10.1109/TMTT.2009.2032345.

[40] A. A. Immorlica et al., "Miniature 3D micro-machined solid state power amplifiers," in *Proc. 2008 IEEE Int. Conf. Microw., Commun., Antennas Electron. Syst.*, pp. 1–7, doi: 10.1109/COMCAS.2008.4562783.

[41] J. Butler, "Beam-forming matrix simplifies design of electronically scanned antennas," *Electron. Des.*, vol. 9, pp. 170–173, Apr. 1961.

[42] L. M. Abdelghani, T. Denidni, and M. Nedil, "Ultra-broadband 4×4 compact Butler matrix using multilayer directional couplers and phase shifters," in *Proc. 2012 IEEE/MTT-S Int. Microw. Symp. Dig.*, pp. 1–3, doi: 10.1109/MWSYM.2012.6259533.

[43] A. Moscoso-Mártir, I. Molina-Fernández, and A. Ortega-Moñux, "Wideband slot-coupled Butler matrix," *IEEE Microw. Compon. Lett.*, vol. 24, no. 12, pp. 848–850, 2014, doi: 10.1109/LMWC.2014.2303167.

[44] K. Wincza, S. Gruszczynski, and K. Sachse, "Ultrabroadband 4 × 4 Butler matrix with the use of multisection coupled-line directional couplers and phase shifters," in *Proc. 2011 Microw., Radar Remote Sens. Symp.*, pp. 118–122, doi: 10.1109/MRRS.2011.6053615.

[45] S. Karamzadeh, V. Rafii, M. Kartal, and B. S. Virdee, "Compact and broadband 4x4 SIW Butler matrix with phase and magnitude error reduction," *IEEE Microw. Compon. Lett.*, vol. 25, no. 12, pp. 772–774, 2015, doi: 10.1109/LMWC.2015.2496785.

[46] K. Wincza and S. Gruszczynski, "A broadband 4x4 Butler matrix for modern-day antennas," in *Proc. 2005 Eur. Microw. Conf.*, vol. 2, pp. 4–1334, doi: 10.1109/EUMC.2005.1610181.

[47] S. S. Madeti et al., "Broadband 8–12 GHz 8 × 8 modified Butler matrix," in *Proc. 2021 SoutheastCon.*, pp. 1–6, doi: 10.1109/SoutheastCon45413.2021.9401867.

[48] R. De Lillo, "A high performance 8-input, 8-output Butler matrix beamforming network for ultra-broadband applications," in *Proc. IEEE Antennas Propag. Soc. Int. Symp.*, vol. 1, pp. 474–477, 1993.

[49] A. Margomenos et al., "Wafer-level packaging method incorporating embedded thermal management for GaN-based RF front-ends," in *Proc. 14th Intersoc. Conf. Thermal Thermomech. Phenomena Electron. Syst. (ITherm)*, 2014, pp. 976–981, doi: 10.1109/ITHERM.2014.6892387.

[50] J. A. Estrada, G. Lasser, M. Pinto, F. Herrault, and Z. Popović, "Metal-embedded chip assembly processing for enhanced RF circuit performance," *IEEE Trans. Microw. Theory Techn.*, vol. 67, no. 9, pp. 3537–3546, 2019, doi: 10.1109/TMTT.2019.2931010.

[51] L. F. Marzall, P. Danielson, G. Lasser, and Z. Popovic, "Broadband small-aperture high-gain ridge horn antenna array element," *IEEE Antennas Wireless Propag. Lett.*, vol. 20, no. 5, pp. 708–712, 2021, doi: 10.1109/LAWP.2021.3060779.

[52] B. Pollard and G. Sadowy, "Next generation millimeter-wave radar for safe planetary landing," in *Proc. 2005 IEEE Aerosp. Conf.*, pp. 1213–1219, doi: 10.1109/AERO.2005.1559412.

[53] R. Reese, M. Jost, H. Maune, and R. Jakoby, "Design of a continuously tunable W-band phase shifter in dielectric waveguide topology," in *Proc. 2017 IEEE MTT-S Int. Microw. Symp. (IMS)*, pp. 180–183, doi: 10.1109/MWSYM.2017.8058991.

[54] N. Jastram and D. S. Filipovic, "Wideband multibeam millimeter wave arrays," in *Proc. 2014 IEEE Antennas Propag. Soc. Int. Symp. (APSURSI)*, pp. 741–742, doi: 10.1109/APS.2014.6904700.

[55] R. M. Robertson, *Variable Width Waveguide Scanners for Eagle (AN/APQ-7) and GCA (AN/MPN-1)*. Cambridge, MA, USA: MIT Radiation Laboratory, 1946.

[56] N. Ehsan, "Broadband microwave lithographic 3D components," Ph.D. dissertation, Univ. Colorado, Boulder, CO, USA, 2010.

[57] E. D. Cullens, L. Ranzani, K. J. Vanhille, E. N. Grossman, N. Ehsan, and Z. Popovic, "Micro-fabricated 130–180 GHz frequency scanning waveguide arrays," *IEEE Trans. Antennas Propag.*, vol. 60, no. 8, pp. 3647–3653, 2012, doi: 10.1109/TAP.2012.2201089.

[58] L. Ranzani, E. D. Cullens, D. Kuester, K. J. Vanhille, E. Grossman, and Z. Popović, "W-band micro-fabricated coaxially-fed frequency scanned slot arrays," *IEEE Trans. Antennas Propag.*, vol. 61, no. 4, pp. 2324–2328, 2013, doi: 10.1109/TAP.2012.2232637.

[59] L. Ranzani, D. Kuester, K. J. Vanhille, A. Boryssenko, E. Grossman, and Z. Popović, "G-band micro-fabricated frequency-steered arrays with 2°/GHz beam steering," *IEEE Trans. THz Sci. Technol.*, vol. 3, no. 5, pp. 566–573, 2013, doi: 10.1109/TTHZ.2013.2271381.

[60] M. A. Elmansouri, L. B. Boskovic, and D. S. Filipovic, "Compact wideband dual-polarized in-band full-duplex antenna subsystem," *IEEE Trans. Antennas Propag.*, vol. 69, no. 11, pp. 7166–7172, 2021, doi: 10.1109/TAP.2021.3050570.

[61] S. Tanaka, N. Shimomura, and K. Ohtake, "Active circulators—The realization of circulators using transistors," *Proc. IEEE*, vol. 53, no. 3, pp. 260–267, Mar. 1965, doi: 10.1109/PROC.1965.3683.

[62] S. K. Cheung, T. P. Halloran, W. H. Weedon, and C. P. Caldwell, "MMIC-based quadrature hybrid quasi-circulators for simultaneous transmit and receive," *IEEE Trans. Microw. Theory Techn.*, vol. 58, no. 3, pp. 489–497, 2010, doi: 10.1109/TMTT.2010.2040325.

[63] L. Marzall, S. Verploegh, T. Cappello, M. Roberg, and Z. Popović, "Active MMIC circulator performance in a phased-array-like environment," in *Proc. 2020 IEEE 50th Eur. Microw. Conf.* (EuMC), 2021, pp. 1186–1189, doi: 10.23919/EuMC48046.2021.9338071.

[64] M. Kunes and G. Connor, "A digitally controlled tunable high power output filter for space applications," in *Proc. 1989 19th Eur. Microw. Conf.*, pp. 681–686, doi: 10.1109/EUMA.1989.334047.

[65] D. Psychogiou, R. Gómez-García, and D. Peroulis, "A class of fully-reconfigurable planar multi-band bandstop filters," in *Proc. 2016 IEEE MTT-S Int. Microw. Symp. (IMS)*, pp. 1–4, doi: 10.1109/MWSYM.2016.7540362.

[66] T. Yang and G. M. Rebeiz, "Bandpass-to-bandstop reconfigurable tunable filters with frequency and bandwidth controls," *IEEE Trans. Microw. Theory Techn.*, vol. 65, no. 7, pp. 2288–2297, 2017, doi: 10.1109/TMTT.2017.2679182.

[67] S. Reynolds, P. Pepeljugoski, J. Schaub, J. Tierno, and D. Beisser, "A 7-tap transverse analog-FIR filter in 0.12 µm CMOS for equalization of 10Gb/s fiber-optic data systems," in *Proc. ISSCC. 2005 IEEE Int. Dig. Tech. Papers Solid-State Circuits Conf.*, vol. 1, pp. 330–601, doi: 10.1109/ISSCC.2005.1494003.

[68] J. Lee and A. Freundorfer, "MMIC adaptive transversal filtering using Gilbert cells and is suitable for high-speed lightwave systems," *IEEE Photon. Technol. Lett.*, vol. 12, no. 2, pp. 196–198, 2000, doi: 10.1109/68.823515.

[69] A. Momtaz and M. M. Green, "An 80 mw 40 Gb/s 7-tap t/2-spaced feed-forward equalizer in 65 nm CMOS," *IEEE J. Solid-State Circuits*, vol. 45, no. 3, pp. 629–639, 2010, doi: 10.1109/JSSC.2009.2039268.

[70] G. Lasser, R. Langwieser, R. Dallinger, and C. F. Mecklenbräuker, "Broadband leaking carrier cancellation for RFID systems," in *Proc. 2012 IEEE/MTT-S Int. Microw. Symp. Dig.*, pp. 1–3, doi: 10.1109/MWSYM.2012.6259548.

[71] J. R. Montejo-Garai, L. Marzall, and Z. Popović, "Octave bandwidth high-performance microstrip-to-double-ridge-waveguide transition," *IEEE Microw. Compon. Lett.*, vol. 30, no. 7, pp. 637–640, 2020, doi: 10.1109/LMWC.2020.3000283.

[72] J. Howell, "Phased array alignment and calibration techniques," in *Proc. Workshop Test. Phased Arrays Diagnostics*, 1989.

[73] E. Lier, M. Zemlyansky, D. Purdy, and D. Farina, "Phased array calibration and characterization based on orthogonal coding: Theory and experimental validation," in *Proc. 2010 IEEE Int. Symp. Phased Array Syst. Technol.*, pp. 271–278, doi: 10.1109/ARRAY.2010.5613357.

[74] C. L. Holloway et al., "Broadband Rydberg atom-based electric-field probe for si-traceable, self-calibrated measurements," *IEEE Trans. Antennas Propag.*, vol. 62, no. 12, pp. 6169–6182, 2014, doi: 10.1109/TAP.2014.2360208.

[75] A. K. Robinson, N. Prajapati, D. Senic, M. T. Simons, and C. L. Holloway, "Determining the angle-of-arrival of a radio-frequency source with a Rydberg atom-based sensor," *Appl. Phys. Lett.*, vol. 118, no. 11, p. 114,001, 2021, doi: 10.1063/5.0045601.

[76] J. A. Sedlacek, A. Schwettmann, H. Kübler, R. Löw, T. Pfau, and J. P. Shaffer, "Microwave electrometry with Rydberg atoms in a vapour cell using bright atomic resonances," *Nature Phys.*, vol. 8, no. 11, pp. 819–824, 2012, doi: 10.1038/nphys2423.

[77] K.-Y. Liao et al., "Microwave electrometry via electromagnetically induced absorption in cold Rydberg atoms," *Phys. Rev. A*, vol. 101, no. 5, p. 053432, 2020, doi: 10.1103/PhysRevA.101.053432.

[78] C. S. Adams, J. D. Pritchard, and J. P. Shaffer, "Rydberg atom quantum technologies," *J. Phys. B, At., Mol. Opt. Phys.*, vol. 53, no. 1, p. 012002, 2019, doi: 10.1088/1361-6455/ab52ef.

[79] P. Asbeck and Z. Popovic, "ET comes of age: Envelope tracking for higher-efficiency power amplifiers," *IEEE Microw. Mag.*, vol. 17, no. 3, pp. 16–25, 2016, doi: 10.1109/MMM.2015.2505699.

[80] M. R. Duffy, G. Lasser, G. Nevett, M. Roberg, and Z. Popović, "A three-stage 18.5–24-GHz GaN-on-SiC 4 w 40% efficient MMIC PA," *IEEE J. Solid-State Circuits*, vol. 54, no. 9, pp. 2402–2410, 2019, doi: 10.1109/JSSC.2019.2924087.